Spin and Charge

Spintronics
Electrical and Optical Properties of Quantum Structures and Devices

Spintronics in Layered Magnetic Structures

INTRODUCTION

Electronic devices rely on the electric charge of electrons, which allows the control of the current flow by electric fields. The spin is another fundamental property of the electron and causes its magnetic moment. The electronic spin gives rise to the magnetism of solids, but also provides a means to influence the electrons by a magnetic field. Thus, in ferromagnetic (FM) materials the motion of an electron may depend on its spin orientation with respect to the local magnetisation. This gives rise to interesting new effects which belong to the field of spintronics or magnetoelectronics. They occur on a length scale on which the spin is conserved, the so-called spin diffusion length, which is of the order of a few nanometers (e.g. several nm for Cr). Therefore thin films, multilayers, and interfaces play a crucial role for spintronics. The most prominent magnetotransport phenomenon is the giant magnetoresistance (GMR) effect. It describes the observation that in layered magnetic structures consisting of thin FM and non-FM metallic layers the electric resistivity depends on the relative alignment of the magnetisations of adjacent FM layers. As an external magnetic field can modify this alignment, the GMR effect provides a simple and efficient way to measure magnetic fields. The GMR magnetic field sensors led to the widespread application of the GMR effect in read heads of hard disc drives within only one decade after the discovery.

APPROACH

We prepare magnetic layered structures of various material combinations by molecular-beam epitaxy (MBE) and sputter deposition. Optical and electron-beam lithography is used to microstructure junctions and nanocontacts. Various methods are used to characterise structural, electronic, magnetic, and transport properties of the samples. We aim at

- a fundamental understanding of magnetotransport phenomena,
- developing new materials and material combinations, and
- observing new effects and functionalities for device applications.

First observations of the GMR

The GMR effect was independently discovered in the late 80´ies by Peter Grünberg (IFF, FZJ) and Albert Fert (Université Paris-Sud). Both groups used layered Fe/Cr structures (Fig. 1). At zero field, adjacent Fe layers align antiparallel due to antiferromagnetic (AF) interlayer exchange coupling across Cr (yet another groundbreaking discovery made at the Forschungszentrum Jülich [1]), whereas an external magnetic field forces the Fe layer magnetisations into a parallel configuration. This transition is accompanied by a drastic change of the electrical resistance. If R_P denotes the resistance for parallel magnetisation alignment and R_{AP} the resistance for the antiparallel state, then the strength of GMR effect is usually quoted in terms of

$$\Delta R/R_P = (R_{AP} - R_P) / R_P.$$

In Fig. 1, $\Delta R/R_P$ amounts to 1.5% for the Fe/Cr/Fe trilayer measured at room temperature and up to 80% at 4.2 K for Fe/Cr superlattices. Nowadays, several 10% at room temperature are commonly observed. The blue line in Fig. 1a shows the anisotropic magnetoresistance (AMR), the predecessor of the GMR effect in read head sensors, for an equivalent Fe thickness. The much larger response is the key advantage of GMR, which paved the way for a significant increase of the storage density of hard disc drives.

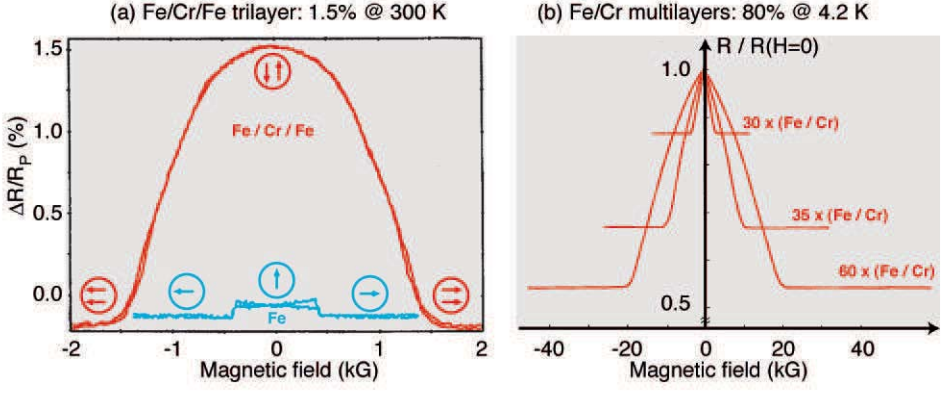

Fig. 1
First observations of the GMR effect
(a) for a Fe / Cr / Fe trilayer and (b) for various Fe/Cr multilayers. The blue curve in (a) shows the AMR signal of a 25 nm-thick Fe film. Arrows indicate the relative alignment of the film magnetisations [1].

Roughness-induced enhancement of the GMR

GMR is related to the spin-asymmetry of spin-dependent scattering. Surprisingly, there it is still a debate whether the relevant scattering centres are located at the FM/non-FM interfaces or in the bulk of the FM films. Therefore, we prepared identical samples, except for small and well-defined differences in interface roughness. This is achieved by measuring reflection high-energy diffraction (RHEED) intensity oscillations during the deposition of epitaxial Fe/Cr/Fe(001) trilayers by MBE: Stopping the deposition at a low or high RHEED intensity corresponds to a higher or lower surface roughness as sketched in Fig. 2. The Cr spacer thickness is fixed at 9 atomic layers. Thus, we obtain "smooth" and "rough" samples, which are almost identical, the only difference being their interface roughness. Magneto-optical Kerr-effect (MOKE) remagnetisation measurements show that in all samples the magnetisations of the two Fe layers are AF coupled, as expected for a Cr spacer of 9 atomic layers thickness, and can be aligned parallel in a field of about 120 mT. In order to measure the GMR with the current applied in the plane of the layers, the samples are micro-structured using optical lithography. Normalised magnetoresistance curves obtained at room temperature from a pair of "rough" and "smooth" samples are shown in Fig. 3. The sample

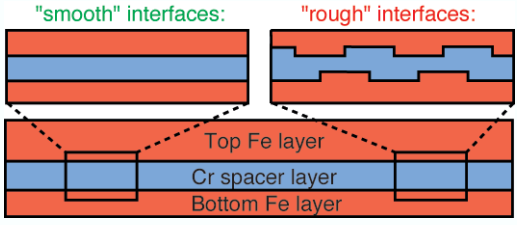

Fig. 2
Schematic of samples with smoother (left) or rougher (right) interfaces obtained by stopping the film deposition of the bottom Fe layer and the Cr at maximum (left) or minimum (right) RHEED intensity.

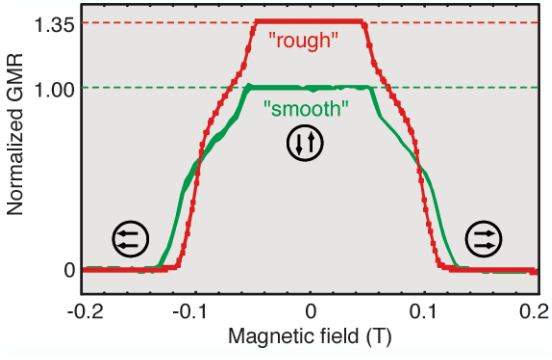

Fig. 3
Magnetoresistance of "smooth" (green curve) and "rough" (red curve) samples according to Fig. 2. Samples with "rough" interfaces show a stronger GMR effect [2].

with rougher interfaces reveals a GMR, which is enhanced by a factor of 1.35 compared to the "smooth" sample. This result emphasises the importance of spin-dependent scattering at the FM/spacer interfaces for the GMR since only the interfaces are weakly modified in this experiment. We conclude, that interface roughness increases the number of spin-dependent scattering sites and, therefore, leads to an enhancement of the GMR.

Coexistence of electronic tunneling and strong anti-ferromagnetic coupling through Si layers

It is well established that the magnetic interlayer coupling across metallic, conductive spacers is connected with an indirect RKKY-type exchange and that it oscillates from FM to AF as a function of spacer thickness. The situation is less clear for non-conductive spacer layers, i.e. semiconductors or insulators.
We use the co-deposition of Fe and Si to prepare epitaxial $Fe_{1-x}Si_x$ spacers of different conductivity by varying concentration x in the range from x=0.5 to x=1, corresponding to a transition from a metallic silicide phase to nominally pure Si. The inset in Fig. 4 shows a cross-sectional transmission electron microscopy image of a Fe/Si/Fe structure. The Si spacer appears as a bright stripe and forms sharp interfaces with the Fe layers. The effect of increasing the Si content in the $Fe_{1-x}Si_x$ spacers on the coupling strength J_1 is displayed in Fig. 4: The coupling increases by

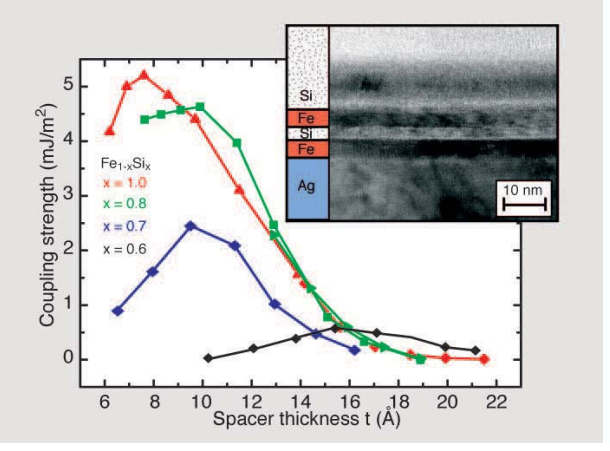

Fig. 4
Coupling strength versus spacer thickness of Fe/$Fe_{1-x}Si_x$/Fe trilayers for various compositions x. The coupling is strongest for nominally pure Si spacers [2]. Inset: TEM image of a Fe/Si/Fe structure.

almost one order of magnitude. For nominally pure Si it reaches values, which belong to the largest ever found. This surprising and theoretically nonunderstood observation is most likely related to the presence of a non-conductive spacer. The coupling does not oscillate with spacer thickness as in the case of metallic spacers, but decays on a characteristic length of only about 2 Å, similar to the decay of a wave function inside a tunneling barrier.

Evidence for the presence of a tunneling barrier is provided by electric transport measurements (Fig. 5). The voltage dependence of a current flowing perpendicular to the sample plane (CPP-geometry) shows the typical characteristics of tunneling and can be fitted by the Brinkman formula. The resistivity of Fe/Si/Fe trilayers is 10^5 times larger than the resistivity of pure Fe. Additionally, the temperature dependence of the CPP-resistance shows the typical behaviour of an insulator (inset of Fig. 5). Therefore, we have shown that strong AF coupling and transport via tunneling coexist in epitaxial Fe/Si/Fe structures. This new combination of properties permits new device concepts with advanced functionality.

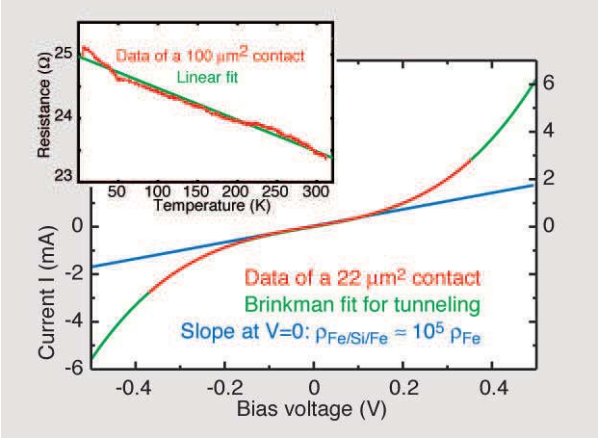

Fig. 5
The I-V characteristics of a Fe/Si/Fe contact and its Brinkman fit as well as the absolute resistance and its temperature dependence (inset) suggest the presence of a non-conducting spacer [3].

Current-induced magnetic switching

The spin-dependence of the electron´s motion leads to another interesting effect, namely the non-equilibrium exchange interaction. This permits current-induced magnetic switching. Whereas the magnetisation alignment is used to control the current flow in GMR devices, the situation is reversed for current-induced switching: Here, the magnetisation alignment is controlled by the direction of an electric current. This new effect is expected to provide a much simpler scheme for the writing process of GMR based magnetic random access memories (MRAM).

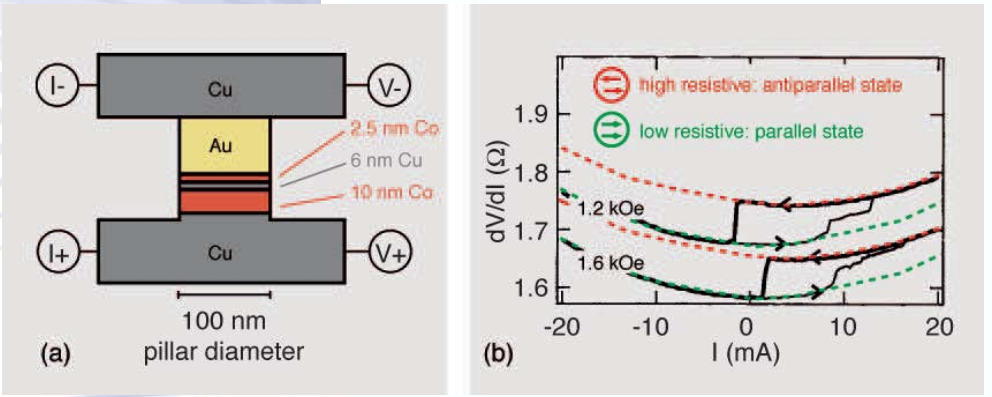

Fig. 6
(a) Side view of the pillar structure used for the observation of current-induced magnetic switching. (b) GMR measurement showing the switching behaviour for two different external magnetic field strengths [J.A. Katine et al., Phys. Rev. Lett. 84, 3149 (2000)].

First observations of current-induced switching in pillar devices were reported by the Cornell group. The sample consisted of a thin (2.5 nm) and a thick (10 nm) Co layer with a 6 nm thick Cu spacer in between and was entirely poly-crystalline. Thick Cu and Au layers are used as leads (Fig. 6a). The current flows through the leads I^- and I^+, and the voltage is measured at V^- and V^+. The diameter of the pillar is only 100 nm. This extreme lateral constriction is required to obtain the necessary high current density (10^8 A/cm^2) to establish a non-equilibrium situation. The relative orientation of the Co layers is measured via the GMR effect of the Co/Cu/Co trilayer (Fig. 6b). When the electrons flow from the thick to the thin Co layer, the parallel alignment is stabilised yielding a low resistivity dV/dI. At reversed current direction, the parallel alignment is destabilised, the thin Co layer switches to

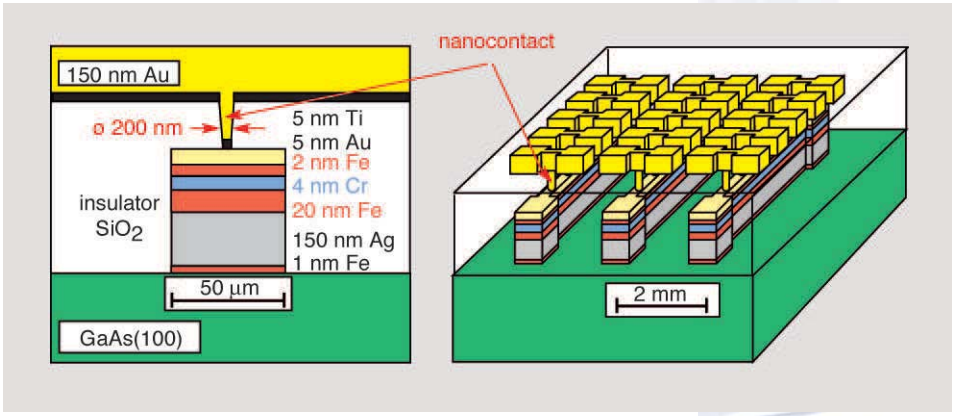

Fig. 7
Layer succession and wafer layout for the nanocontacts prepared at the Forschungszentrum Jülich. The single-crystalline active layers (Fe/Cr/Fe) are grown by MBE.

the antiparallel alignment at a sufficiently large current, and dV/dI increases. We are extending the study of current-induced magnetic switching to

- alternative material combinations (e.g. Fe/Cr) and to
- single-crystalline structures in order to enlarge the experimental data base needed for a comparison with competing theoretical models.

Figure 7 shows on the left side the succession of the epitaxial layers and the constriction forming a nanocontact, from which the current will be injected very locally. The right hand side shows the layout of 15 nanocontacts and the corresponding contact pads on a wafer. A combination of MBE, electron-beam and optical lithography is used to define these structures. Atomic force microscopy (AFM) images (Fig. 8) and first transport measurements, which reveal metallic conductivity, prove the successful formation of nanocontacts. Magnetic and magnetotransport characterisation experiments are under way.

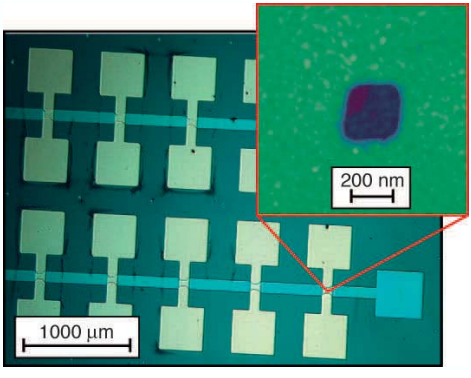

Fig. 8
Photograph of the structured sample. The nanocontacts are located at the crossing of the bottom (blue) and top (green) electrodes. Inset: AFM image of a lithographically defined hole taken prior to the deposition of the top Au electrode.

REFERENCES

[1] "Layered Magnetic Structures: History, Highlights, Applications"
P. Grünberg
Physics Today, May 2001, p. 31.

[2] "Experiments on the relation between GMR and interface roughness and on the interlayer exchange coupling across semiconductors"
P. Grünberg, D.E. Bürgler, R. Gareev, D. Olligs, M. Buchmeier, M. Breidbach, B. Kuanr, and R. Schreiber
J. Phys. D: Appl. Phys. **35** (2002) 2403.

[3] "Exchange coupling across metallic and semiconducting interlayers"
D.E. Bürgler, M. Buchmeier, S. Cramm, S. Eisebitt, R.R. Gareev, P. Grünberg, C.L. Jia, L.L. Pohlmann, R. Schreiber, M. Siegel, Y.L. Qin, and A. Zimina
J. Phys.: Condens. Matter, 15 (2003) S443.

AUTHORS

Daniel E. Bürgler and Peter A. Grünberg

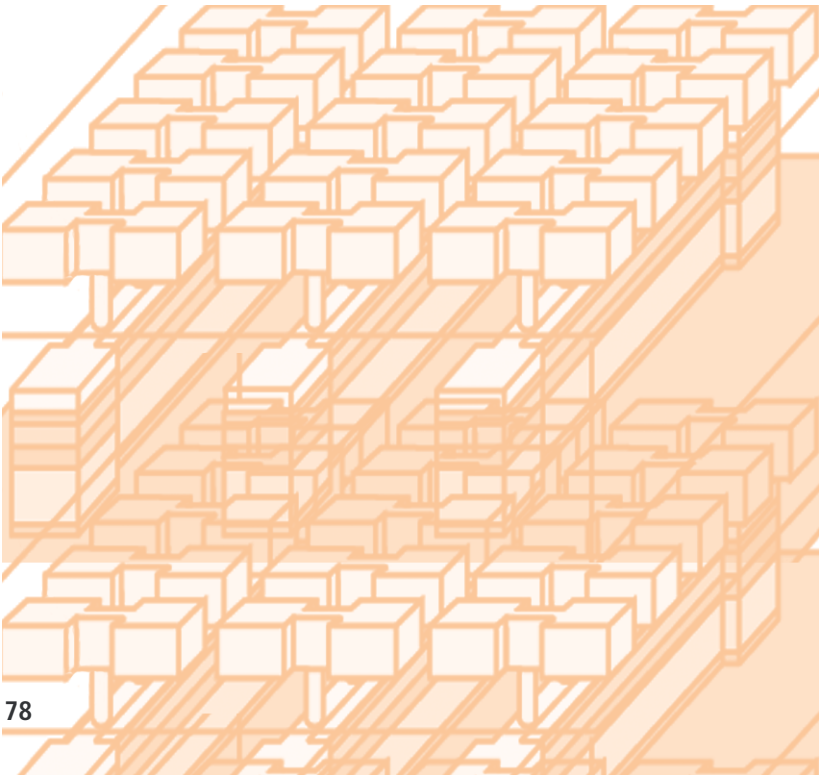

Multilayers for Magnetoelectronics

INTRODUCTION

The discovery of the giant magnetoresistance (GMR) effect and the development of GMR sensors for reading heads of hard disc memories is a well known Jülich success story. The magnetoresistive (MR) effects are much stronger within heterostructures than in homogenous films. One needs alternating, thin layers of ferromagnetic and non-magnetic metals to obtain the giant magnetoresistance (GMR). In these heterostructures the current flow is strongly affected by the relative orientation of the magnetic moments within the magnetic layers. One decade after the discovery of the GMR effect, magnetic reading heads based on the GMR are on the market. Other applications of the GMR are magnetic sensors, magnetic random access memories (MRAM), spin valves, robotics and automobile electronics. An improvement of the MR effects is expected from new multilayers and from the detailed control and understanding of growth, structure, and interface properties on the atomic scale. In addition, new physics is observed in tunneling experiments. The tunneling resistance (TMR) between two ferromagnetic metal layers separated by a thin insulator (an Al_2O_3 tunneling barrier, e.g.) depends on the relative orientation of the magnetization of ferromagnetic layers.

APPROACH

We investigate different material systems used for GMR and TMR devices in order to improve the knowledge on their thin film structure and growth properties. As the film thickness is limited to a few nanometers, the morphology of the layers and interfaces has a significant influence on the electronic properties. Our multilayer systems are grown under ultrahigh vacuum (UHV). They are studied in situ by scanning tunneling microscopy (STM), low energy electron diffraction (LEED), Auger electron spectroscopy (AES), high-resolution electron energy loss spectroscopy (EELS), scattering of Helium atoms (TEAS) and magnetooptical Kerr effect (MOKE). We are focussing our research on the influence of the structural details on the electrical and

RESULTS

magnetic properties. Based on our experience in the growth of epitaxial oxide phases on metallic surfaces (NiAl, CoGa), we are now establishing new procedures for the growth of oxide films on magnetic substrates. Although commonly Al oxides are used as tunneling barriers in TMR devices, we will also study Ga oxide or a combination of Ga oxide and Al oxide.

β-Ga_2O_3-CoGa(100)

We have studied the growth of Ga oxide on the CoGa(100) surface. Oxidation in the temperature range between 700 – 900 K leads to the formation of an ordered β-Ga_2O_3 with an uniform thickness of about 1nm. Basically Ga atoms segregate to the surface and react with adsorbed oxygen atoms, a process which

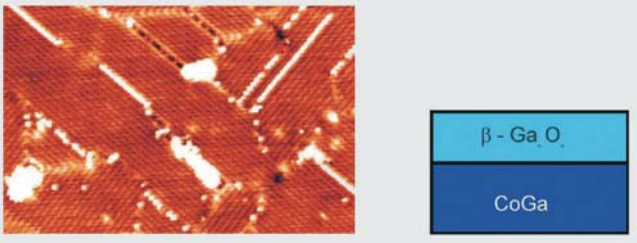

Fig. 1
STM image of a β-Ga_2O_3 grown at 700 K on a CoGa(100) surface. The image shows an area of 400 x 255 $Å^2$.

is called "preferential segregation epitaxy".
After completion of the first oxide layer, further segregation of Ga atoms is suppressed and the growth of the oxide film stops. As shown in the STM image (Fig. 1) an oxide surface grown at 700 K is well ordered, the distance between the streaks is 5.6 Å, which corresponds to the distance between the Ga rows of the top layer of β-Ga_2O_3. One observes two domains perpendicular to each other and, in addition, antiphase domain boundaries which are imaged sometimes as protrusions (rows of white dots) and sometimes as depressions (dark). The larger white structures are small oxide domains which stick out 3 Å above the terrace. By oxidation at 900 K, the individual domains grow to a tenfold larger size and the small oxide islands, which were sticking out of the terraces, have disappeared.

$Fe(Co)/Fe_2O_3/Fe/Cu(110)$

The deposition of 5 monolayers Fe at 130 K on Cu(110) and subsequent annealing to 240 K leads to the formation of a well ordered fcc γ-Fe(110) film. He scattering shows that the smoothness of this Fe film is almost the same as that of the clean Cu(110) surface. Adsorption at 130 K followed by annealing at around 500 K leads to the epitaxial growth of an ordered Fe_2O_3

film on top of the γ-Fe(110) film. The structure of this film (see Fig. 2) can be interpreted in terms of a coincidence lattice of the Cu substrate, respectively the γ-Fe(110) underlayer with a Fe_2O_3 film which is distorted, both parallel and perpendicular to the surface. On the Fe oxide, Fe grows epitaxially in the stable bcc α Fe phase with a (100) orientation. Co is found to grow on the oxide in the fcc phase with (110) and (100) orientations. For both Co phases and for the Fe film the [001] directions are aligned along the [100] direction of the Cu(110) substrate. The distortion of the oxide film, due to the misfit with the substrate, is sufficiently large to make the [100] and [110] axes of the substrate the favoured directions for alignment of the Fe and Co films on the oxide surface.

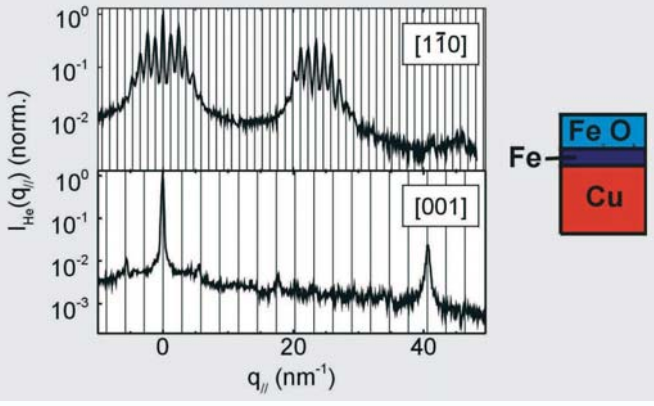

Fig. 2
He diffraction spectra measured on a $Fe_2O_3/Fe/Cu(110)$ surface along the [110] and [001] directions of the copper substrate. The lines correspond to peak positions for a 21x6 superstructure.

Au/Co/Ga_2O_3/Ni(100)

A model structure for TMR has been prepared with Ga_2O_3 as the tunnel barrier. The morphology and growth of the layers have been investigated. On the (100) surface of Ni a c(2x2)-oxygen overlayer was prepared and subsequently a 10 Å thick Ga layer was deposited at 80 K. The Ga layer was oxidized at 80 K and annealed to 700 K. At 700 K the Ga oxide was again exposed to oxygen until saturation as achieved. Afterwards a 30 Å thick Co layer was deposited and annealed at 700 K. During annealing the Co layer rearranges itself to a fcc structure with the (100) plane parallel to the surface. See Fig. 3 for a schematic of the TMR system. In addition, a LEED pattern of the Co layer and a high resolution EEL spectrum of the Ga_2O_3 tunnel barrier is shown. The EEL spectrum exhibits losses at 305, 470, and 745 cm^{-1} (and the corresponding gains at –305, –470 and –745 cm^{-1}) which are assigned to Fuchs-Kliewer phonons of Ga_2O_3. The TMR model system was covered with 50 Å Au in order to study the tunneling properties in collaboration with the Institute for Solid State Physics (IFF). To our surprise the Au film grows in well ordered form with the (111) plane parallel to the surface.

Fig. 3
Schematic of the TMR model system Au/Co/Ga_2O_3/Ni(100). In addition, a LEED pattern of the Co layer and an EEL spectrum of the Ga_2O_3 film are shown.

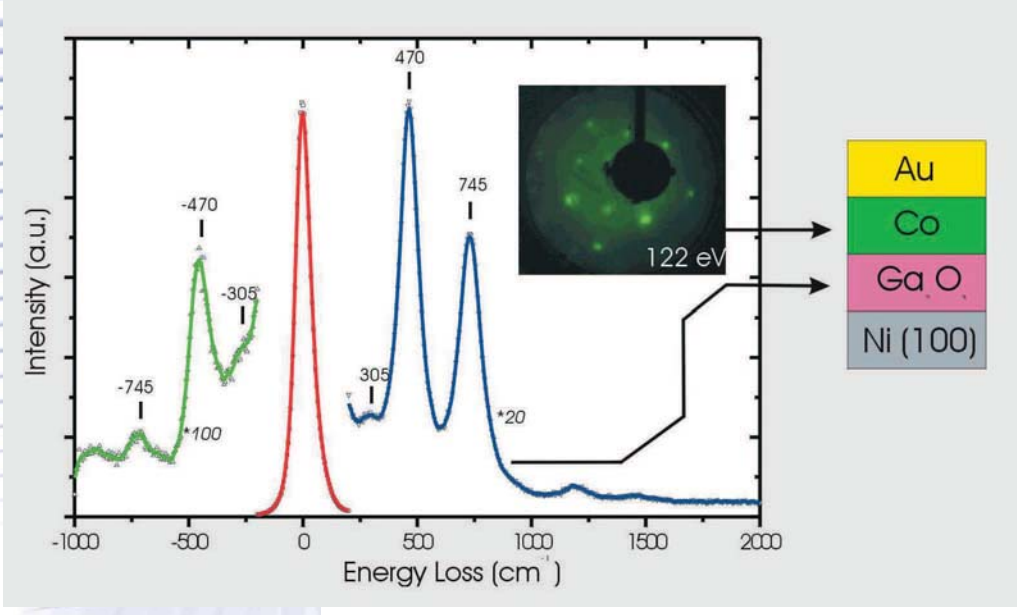

REFERENCES

(1) "Growth of thin, crystalline oxide, nitride and oxynitride films on metal and metal alloy surfaces"
R. Franchy
Surf. Sci. Reports 38(6-8), (2000) 195-294.

(2) "Elemental steps in the growth of thin b-Ga_2O_3 on CoGa(100)"
R. Franchy, M. Eumann and G. Schmitz
Surf. Sci. 470 (2001) 337.

(3) "The band-gap of amorphous and well-ordered Al_2O_3 on $Ni_3Al(100)$"
Ioan Costina and René Franchy
Appl. Phys. Lett. 78 (2001) 4139.

AUTHORS

Rudolf David, Laurens Verheij, René Franchy

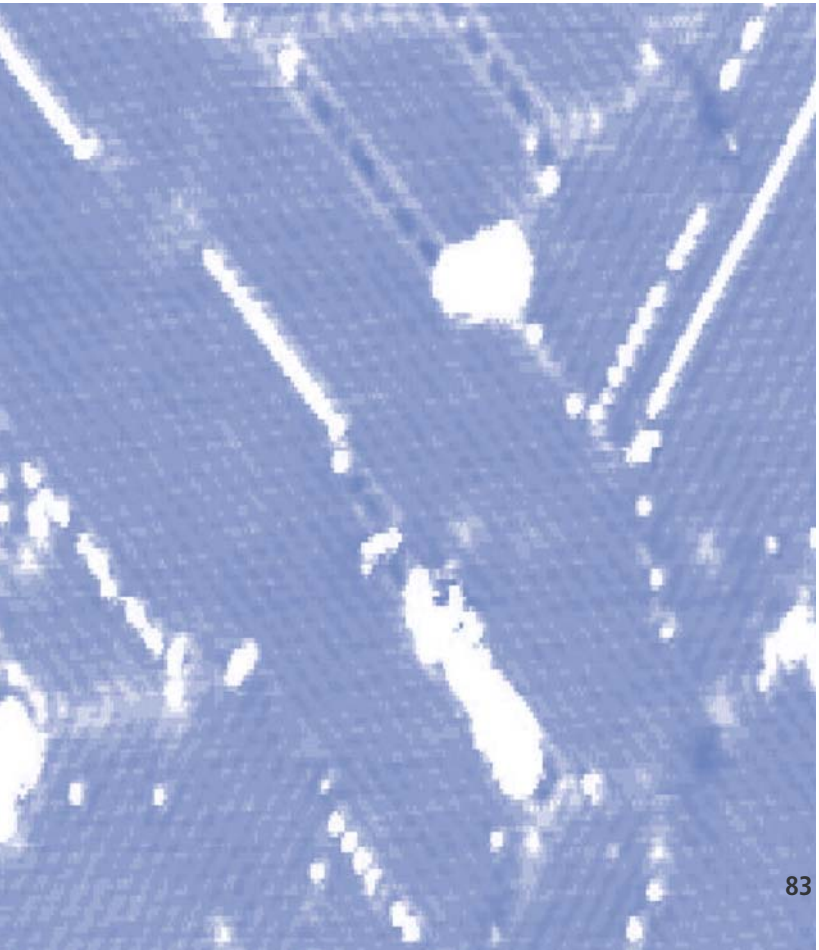

Magnetic Tunnel Junctions

INTRODUCTION

The development of spintronics is discussed by several contributions in this booklet. One of the major goals and challenges is the development of a magnetoresistive random access memory (MRAM). MRAMs are non-volatile, in contrast to conventional DRAMs (dynamic random access memories). An MRAM, however, retains data after the power is cut off, similar to a magnetic hard disk or a floppy disk. Replacing the DRAM by an MRAM could prevent data loss and enable computers that start instantly, without the boot up sequences. In this sense the MRAM would be unique, offering the access time of DRAMs (typically 50 ns) and the non-volatile data-storage of hard disks. Moreover, it is immune to radiation damage, consumes little power, and operates over wide temperature ranges.

The heart of the MRAM is a magnetic tunnel junction (MTJ). Each MTJ stores a single bit of information ("0" and "1"). The

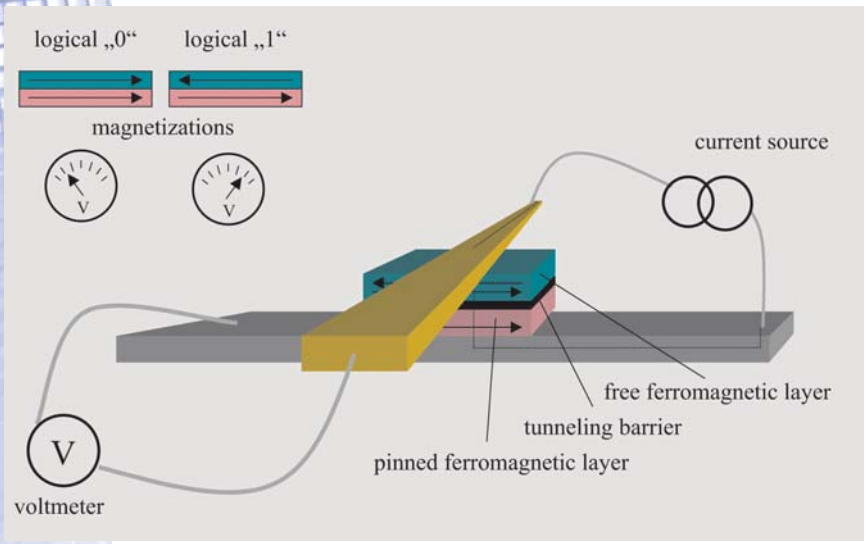

Fig. 1
Schematic of a magnetic tunneling junction (MTJ). The magnetization of the pinned layer is fixed, the magnetization of the free layer can be switched by applying an external magnetic field.

MTJ includes two magnetic layers separated by a thin dielectric barrier [1]. The polarization of one of the magnetic layers is fixed in one direction (Fig. 1). The polarization direction of the free magnetic layer is used for information storage. The resistance of the memory bit is either low or high, depending on the relative polarization (parallel or anti-parallel) of the free layer with respect to the pinned layer. One layer is typically pinned by an adjacent anti-ferromagnetic layer of $Ir_{50}Mn_{50}$. An applied field can switch the free layer only. In an MRAM array, orthogonal lines pass under and over the bit area, carrying an electrical current that produces the switching magnetic field. The design is such, that the film will not switch, if current is applied to just one line, but it will always switch, if current is flowing through both lines, that cross at the selected bit.

The tunneling magnetoresistance can be explained with the help of a two-band model [2]: the d-band is split into spin-up and spin-down bands with a different density of states at the Fermi energy. If the magnetization of the layers is parallel, the majority-band electrons tunnel across the film to the majority band of the opposing electrode and the minority to the minority band.

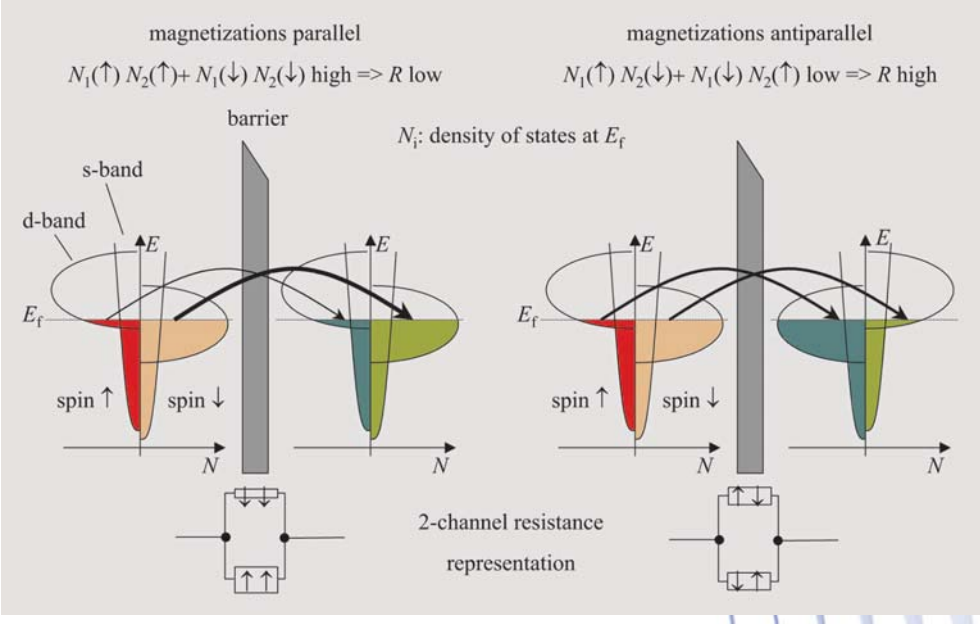

Fig. 2
Simple spin-split d-band-model for tunneling magneto resistance (TMR)

When they are antiparallel, the majority/minority band electrons are forced to tunnel into the minority/majority band of the opposing electrode. The reduced number of states available for tunneling between the antiparallel ferromagnetic layers results in an increased tunneling resistance, as compared to parallel case (Fig. 2).

APPROACH

As always, the experimental reality is somewhat more complicated than the above mentioned simple theoretical picture. In fact, the barrier material also plays a significant role in both the magnitude and the sign of the observed current. However, the simple two-band model is sufficient for understanding the MR of the AlO_x-based junctions considered here. The tunneling MR ratio is defined, in direct analogy with other types of MR, as the difference in resistance between the two states divided by the resistance in the low state. Because the conduction is perpendicular to the layers, the device resistance scales as the inverse of its area.

The two most critical layers in the MTJ stack are the AlO_x tunnel barrier and the free layer. The tunnel barrier is very thin, approximately 2 nm, and the tunneling resistance is exponentially dependent on its thickness. It must be extremely uniform over the wafer, free of pinholes and very smooth, since small variations in the AlO_x thickness result in large variations of the resistance. Uniformity and the absolute resistance of the cell are critical, since the absolute value of the MTJ resistance is compared with a reference cell during the read mode. In patterned bits, the thickness of the free layer is directly related to the field or current, required for switching the bit. A thin free layer less than 50 Å is desirable because it results in low switching fields for low power write operations. For large-scale manufacturing, processes and deposition tools must be developed that provide an unprecedented level of uniformity and reproducibility.
The layers of the MTJ stack are formed by sputter deposition with rates of several Ångstroms per second. Two techniques have been introduced successfully: physical vapor deposition, specifically planar magnetron sputtering, and ion-beam deposition. The best methods for producing the insulating tunnel bar-

rier are not yet evaluated. Various techniques are currently under study throughout the world. To date the best results are found for AlO_x tunnel-barrier layers, which are made by first depositing a metallic aluminum layer, between 0.5 nm and 1.5 nm thick, and then oxidizing it under UV-light irradiation. Additional techniques studied by other groups include oxidation by glow-discharge plasma and atomic-oxygen exposure. Therefore a key issue for the technological breakthrough of MRAMs is the development of MJTs with appropriate ultra-thin Al_2O_3 oxide layers.

Pinning and large tunnel magneto resistance

We study the spin-dependent tunneling through Al_2O_3 prepared by UV-light assisted oxidization of magnetic tunnel junctions. The complete layer sequence is schematically shown in Fig. 3.

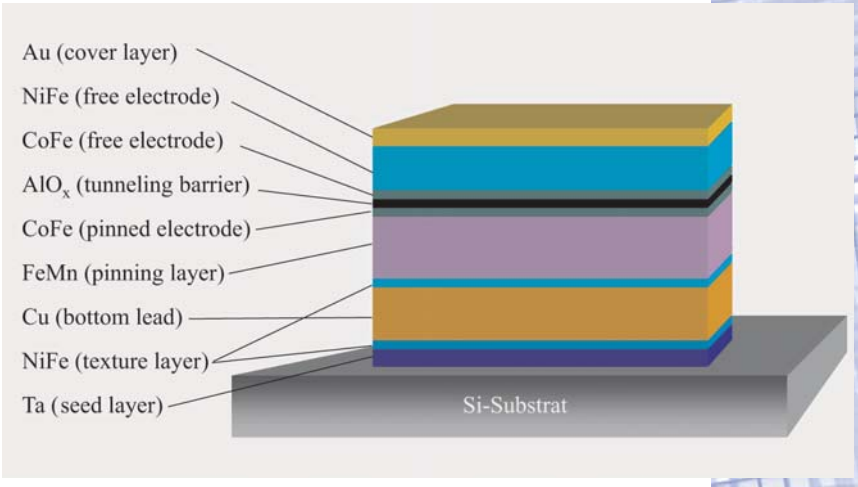

Fig. 3
Schematic stack composition of a MTJ with one pinned electrode.

The first Ta and NiFe were used as a seed and a texture layer respectively for achieving the (111)-direction of the $Fe_{50}Mn_{50}$ layer. It is needed for anti-ferromagnetism and pinning of the adjacent $Co_{75}Fe_{25}$ film (the so-called "exchange-bias"-effect). $Co_{75}Fe_{25}$ was used due the high spin polarization which results in a high magnetoresistance effect. The upper NiFe layer acts as a "driver" to rotate the top $Co_{75}Fe_{25}$ layer with a small magnetic field. MTJs with dimensions down to 1 x 5 μm^2 were patterned

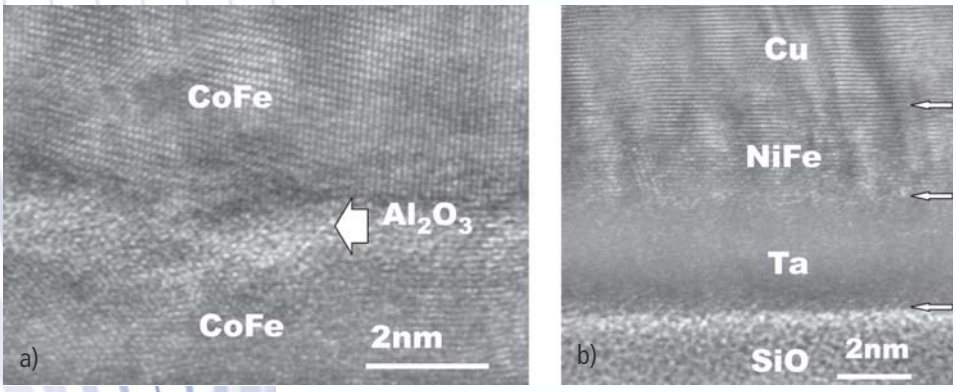

Fig. 4
High resolution transmission electron microscopy (HRTEM) pictures of MTJ stack details.
a) Tunneling barrier and adjacent top and bottom electrodes.
b) Seed and texture layers of MTJ stack.

by a self-aligned microfabrication process using standard optical lithography and ion-beam etching. By using high-resolution transmission microscopy (HRTEM) the individual interfaces of the stack become visible. In Fig. 4(a) the tunnel barrier and the adjacent top and bottom electrodes are shown. The Al_2O_3 tunnel barrier is as thin as 1.5 nm. Although the top and bottom magnetic layer possess a wavy structure, the Al_2O_3 is pinhole free. This is very important, since any pinhole results in a short circuit path between the two metallic electrodes. Figure 4(b) represents the first metallic layer sequence on the silicon substrates. Those layers are needed to achieve a (111) texture in the $Fe_{50}Mn_{50}$ layer, which is a precondition for the pinning the bottom $Co_{75}Fe_{25}$ film.

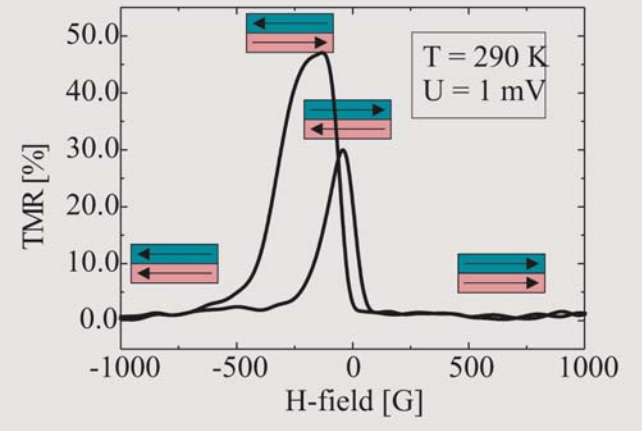

Fig. 5
Magnetoresistance curve of a MTJ at room temperature.

Based on this multilayers MTJs with magnetoresistance values up to 50% at room temperature have been successfully developed. An example of a magnetoresistance measurements is shown in Fig. 5.

Magnons and Traps

In real tunnel barriers, defects in the form of impurities or oxygen vacancies can lead to considerable deviations in the electronic current [2]. The defects form electronic traps. Scattering processes can lead to spin flipping of the electrons. Therefore tunneling via traps may violate spin conservation. A second source for spin flipping is given by magnons at the electrode-barrier interfaces. The generation and annihilation of magnons is accompanied by a spin-flip process. Tunneling via traps as well as magnon excitations may lead to a decrease of the optimal tunneling magnetoresistance. Therefore the barrier and the interfaces both are essential for the fabrication of tunnel junctions with high TMR values. In general the current transport in magnetic tunnel junctions is a complex superposition of different conductivities [3]. The study, understanding and control of these effects is the key to all future MRAM applications.

REFERENCES

[1] S.S.P. Parkin et al., J. Appl. Phys. 85, 5828 (1999).

[2] M. Jullière, Phys. Lett. A 54, 225 (1975).

[3] J. Wingbermühle, S. Stein, and H. Kohlstedt J. Appl. Phys. 92, 7261 (2003).

AUTHORS

Simon Stein, Martin Weides, Hermann Kohlstedt

Computational Spin Electronics

Initiated by the discovery of the Giant Magneto Resistance in 1988 by A. Fert (Paris) and P. Grünberg (Jülich) a new field has emerged, the Magneto or Spin Electronics. This field is now bursting with new phenomena such as halfmetallic ferromagnets with 100% spin polarisation at the Fermi level, spin injection into semiconductors, diluted magnetic semiconductors, current induced magnetisation switching, spin coherent transport in semiconductors. The addition of the spin degree of freedom to the charge-based electronics has led to the vision of a future most powerful spin electronics, with increased information processing speed, nonvolatility, lower power consumption and better scalability. In this document we will briefly describe some theoretical activities in Jülich aiming at a better understanding of this important field. Our calculations are based on density functional theory in the local density approximation, representing the present state of the art in electronic structure calculations. We apply the Korringa-Kohn-Rostoker (KKR) Green function method which to a large extent was developed in Jülich.

1 Tunneling Magneto-resistance

The recent realisation of high Tunneling Junction Magnetoresistance (TMR) by Moodera and Miyazaki has opened the way to new magnetic random access memories (MRAMs) which soon will be introduced into the market. However, understanding the TMR is difficult, in particular for amorphous barriers. In contrast, we are able to give a simple and elegant description for crystalline barriers [1]. In our theory, the decay length of the wavefunction in the insulating gap is a key parameter. The smallest decay parameter corresponds to the largest exponential decay length. This implies that one has to calculate the so-called complex band structure of the semiconductor, and find the state with the smallest imaginary part of the wavevector (decay parameter). As an example, in Figure 1 the decay

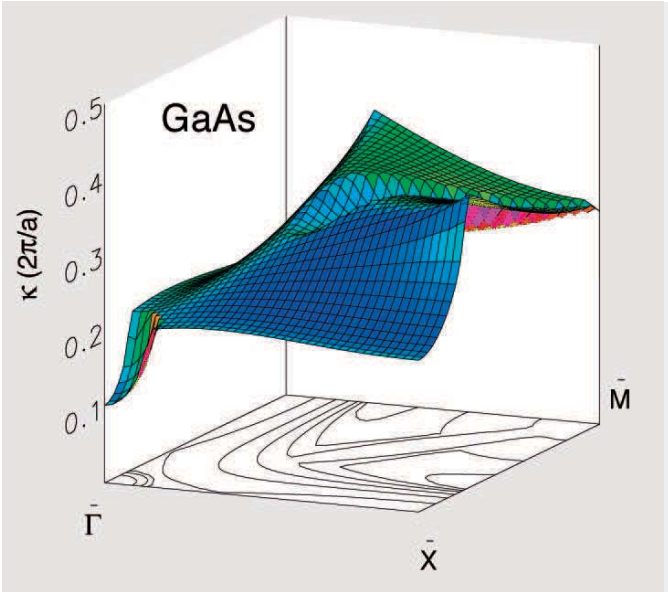

Fig. 1
Decay parameter (inverse exponential decay length) as a function of the in-plane part of the wavevector, for a GaAs (001) barrier.

parameter of GaAs is presented as a function of the in-plane part $k_{||}$ of the wavevector (within the two-dimensional (001) surface Brillouin zone). The Fermi level here has been fixed in the middle of the band gap. The minimum is at $k_{||} = 0$. This state with normal incidence decays slowest and therefore is most important for tunneling. In a second step, one can easily check that, in a clean Fe/GaAs/Fe (001) junction, the majority-spin Fe states couple well to this decaying wavefunction, while the minority-spin states are reflected much stronger because they have incompatible symmetry. As a result, in an antiparallel alignment of the electrodes' moments, both spin directions are strongly reflected (one at each interface) increasing the resistance by orders of magnitude and resulting in a huge TMR. A similar situation is found for ZnSe, Si, and Ge (001).

2 Half-metallic Heusler Alloys

Half-metallic compounds are hybrids between metals and semiconductors, having a band gap at the Fermi level E_F for the one spin direction, but a metallic behaviour for the other one. They were discovered in 1983 by de Groot in ab-initio calculations, but were considered as exotic systems. The development of spin

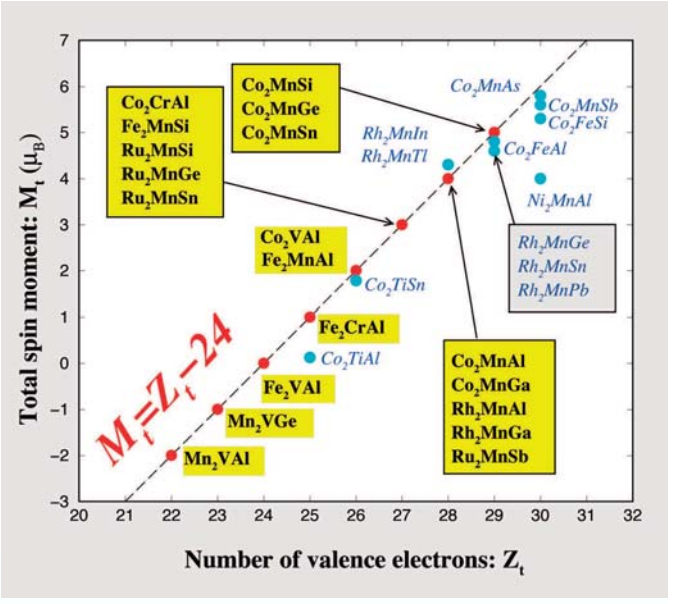

Fig. 2
Calculated total spin moments for all studied Heusler alloys. The dashed line represents the Slater-Pauling behaviour. The blue circles denote ferro-magnetic Heusler alloys which are not half-metallic and have a noninteger total moment, thus deviating from the S-P curve.

electronics and the search for materials with 100% spin polarisation at E_F greatly renewed the interest. Recently we performed a detailed ab-initio study of the electronic structure of half-metallic Heusler alloys, by considering both the half-Heusler compounds of $C1_b$ structure like NiMnSb and the full Heusler compounds with $L2_1$ structure like Co_2MnGe [2]. In particular we have discussed the origin of the gap as arising from the d-d hybridisation between the transition metal atoms. Moreover we derived some simple relations between the total moment M_t per unit cell and the total number Z_t of valence electrons, accounting to $M = Z - 18$ for the half-Heusler and $M_t = Z_t - 24$ for the full-Heusler compounds. The latter "Slater-Pauling" curve for the full-Heusler is shown in Figure 2, demonstrating that the compounds can be classified according to their total moments, taking integer values. Probably there exist many more half-metallic compounds than we have found in our calculations.

3 Diluted magnetic semiconductors

Semiconductors are usually not magnetic. Therefore the recent discovery of ferromagnetism in diluted magnetic semiconductors (DMS) such as InAs and GaAs doped with a few percent of Mn

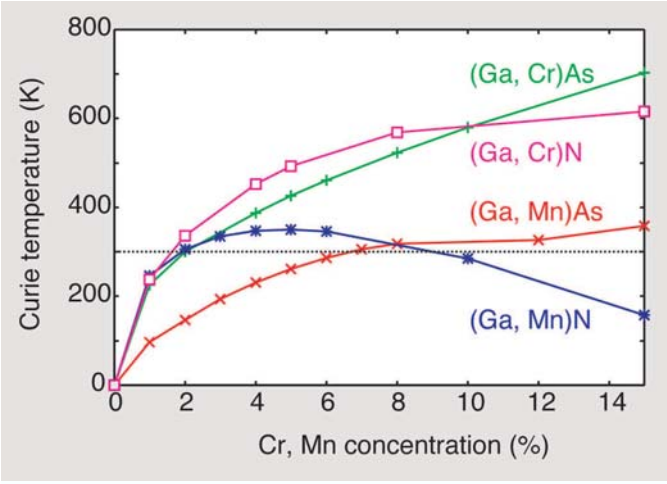

Fig. 3
Calculated Curie temperatures of Crand Mn-doped GaAs and GaN. The dashed line indicates room temperature (300 K).

was an important break-through for spin electronics. However the reported Curie temperatures T_C, e.g., 110 K for (Ga, Mn)As with 5% Mn, are much too low, since for applications T_C -values well above room temperature are needed. In order to propose a

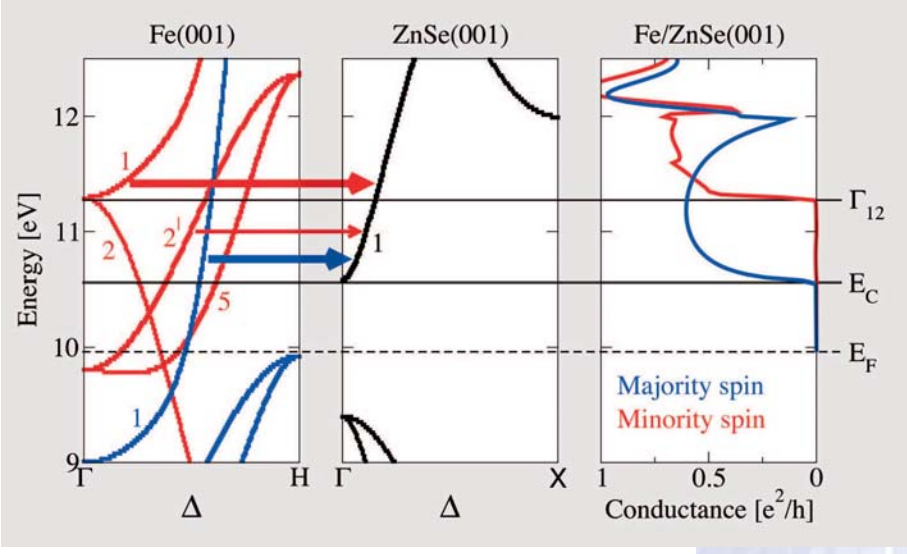

Fig. 4
Band structure of Fe and ZnSe and the conductance through the Fe/ZnSe interface. Blue lines denote the majority and the red ones the minority spin direction. The thickness of the arrows symbolises the coupling strength between the Fe bands and the ZnSe conduction band. The numbers indicate the symmetry character of the bands.

good candidate for high-T_C ferromagnets, we have studied the electronic structure of several DMS in the coherent potential approximation (CPA) and calculated T_C from first-principles in the mean field approximation [3]. As a typical example, the calculated T_C of GaN- and GaAs based DMS are shown in Figure 3 as a function of concentration of transition metal impurities. Very large T_C-values are predicted. In particular, Cr-doped GaN and GaAs are promising candidates with T_C approaching 600 K for realistic Cr-concentrations. Actually, a recent experiment gives for Cr-doped GaN a T_C-value higher than 400 K, so that our prediction seems to be confirmed.

4 Ballistic Spin Injection

The main precondition for a semiconductor-based spin electronics is the successful injection of a spin polarised current in a semiconductor. The ferromagnet Fe seems to be the best candidate, since its bcc lattice fits well to the zinc blende structure of GaAs and ZnSe, thus enabling epitaxial growth. Recently successful injection into GaAs(001) has been demonstrated experimentally, although still with low efficiency. In our theoretical work we have concentrated on this epitaxial system, by considering the spin injection through the perfect Fe/GaAs(001) or Fe/ZnSe(001) interface in the ballistic limit. The resulting conductance has been calculated using the Landauer-Büttiker formalism and the results for "hot" electrons above the Fermi level with perpendicular incidence is shown in Figure 4. Above the conduction band minimum E_C only majority electrons are injected into the semiconductor ZnSe, yielding a nearly 100% spin polarised current. The results can be understood as arising from a symmetry effect of the spin dependent band structure of Fe, being shown on the left side of Figure 4. Only the Fe bands of Δ_1-symmetry can couple well to the conduction band states of the semiconductor and can cross the interface, while the minority states can couple either only very weakly, in the case of the $\Delta_{2'}$-states, or not at all (the Δ_2 and Δ_5 states) [4]. Thus this interface works as a nearly perfect spin filter.

REFERENCES

[1] Ph. Mavropoulos, N. Papanikolaou and P. H. Dederichs, "Complex Band Structure and Tunneling through Ferromagnet/Insulator/Ferromagnet Junctions", Phys. Rev. Lett. 85, 1088 (2000).

[2] I. Galanakis, N. Papanikolaou and P. H. Dederichs, "Origin and Properties of the Gap in the Half-Ferromagnetic Heusler Alloys", Phys. Rev. B 66, 134428 (2002); I. Galanakis, N. Papanikolaou, and P. H. Dederichs, "Slater-Pauling Behavior of the Half-Ferro-magnetic Full-Heusler Alloys", Phys. Rev. B 66, 134429 (2002).

[3] K. Sato, P. H. Dederichs and H. Katayama-Yoshida, "Curie Temperatures of III-V Diluted Magnetic Semi-conductors Calculated from First Principles", submitted to Europhys. Lett. 61, 403 (2003)

[4] O. Wunnicke, Ph. Mavropoulos, R.Zeller, P. H. Dederichs and D. Grundler, "Ballistic spin injection from Fe(001) into ZnSe and GaAs", Phys. Rev. B 65, 241306 (R) (2002).

AUTHORS

Peter Heinz Dederichs, Olaf Wunnicke, Kazunori Sato, Phivos Mavropoulos

Rashba Effect and Quantum Transport in Semiconductor Heterojunctions

INTRODUCTION

In the rapidly developing field of "spintronics", it is not only the electronic charge, but also the electron spin, which is employed as a unit of information. The use of the electron spin may lead to electronic circuits of higher speed and lower power consumption. The additional degree of freedom which is provided by using the control of spin state can add new functionalities to electronic devices. In addition, the spin state in solid-state materials might serve as a basis for the development of quantum computers.

APPROACH

A successful realization of spintronic circuits depends on the design and availability of appropriate material systems. With respect to semiconductor materials, dilute ferromagnetic semiconductors and semiconductor layer systems showing a large spin-orbit coupling are of importance. Concerning the latter, especially in narrow gap semiconductor heterostructures a large spin-splitting can be achieved by utilizing the "Rashba spin-orbit coupling". Here, the macroscopic electric field in the confining quantum well of a two-dimensional electron gas effectively leads to a splitting in two subbands. The spin precession in the two-dimensional electron gas induced by the Rashba effect is proposed as a control mechanism in future spin transistors.

Our investigations on the Rashba effect are based on a strained InGaAs/InP heterojunction grown by metal-organic vapor phase epitaxy. By inserting a strained InGaAs (77% In) layer as a conductive channel very high mobilities are obtained. In order to define the geometry of the semiconductor mesa, reactive ion etching is employed. As an example, a mesa structure of a quantum wire, which was defined by electron beam lithography, is shown in Fig. 1. In some structures the carrier concentration of

the two-dimensional electron gas is controlled by a gate electrode insulated by a SiO_2 layer. In order to study the Rashba effect, magnetotransport measurements in magnetic fields up to 16 T are performed. The samples are usually measured at temperatures below 1 K.

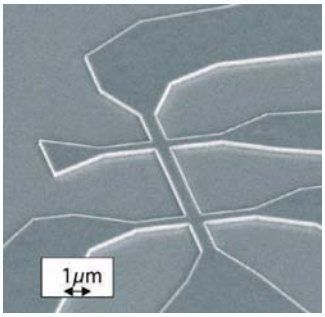

Fig. 1
Scanning electron micrograph of an InGaAs/InP quantum wire structure defined by reactive ion etching.

RESULTS

The spin-splitting in two-dimensional electron gases due to Rashba effect can be observed directly by performing magnetotransport measurements on a Hall bar sample (Fig.2). The resistance shows characteristic oscillations, the so-called Shubnikov-de Haas oscillations, as a function of the magnetic field. The frequency of the Shubnikov-de Haas oscillations gives information on the carrier concentration of the two-dimensional electron gas. As can be seen in Fig. 2, the magnetoresistance shows a characteristic beating pattern owing to two slightly different oscillation frequencies. This directly confirms the existence of two spin-split subbands. The magnitude of the spin splitting can be extracted by analyzing the node positions of the beating pattern. By adjusting the voltage of a gate electrode covering the

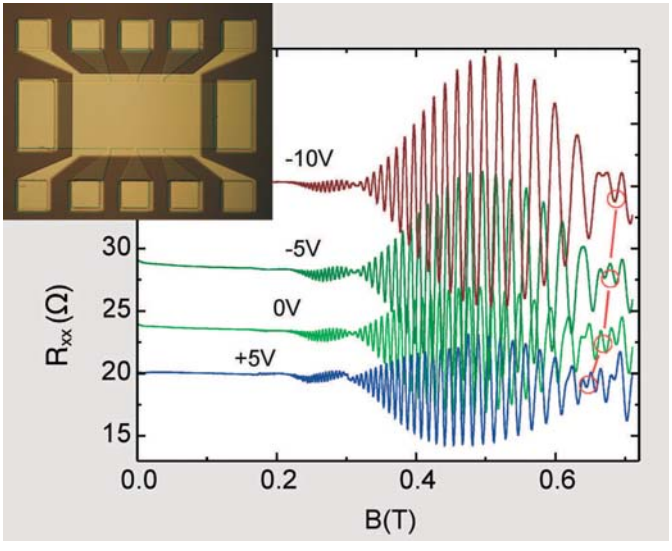

Fig. 2
Shubnikov-de Haas oscillations for various gate voltages. The red circles indicate the shift of the node position with different gate voltages. The small picture shows the Hall bar covered by a gate electrode.

Hall bar, the beating pattern and thus the magnitude of the spin-splitting can be controlled. The control of the spin precession by adjusting the strength of the Rashba effect is one possible mechanism to manipulate the spin state in future spintronic devices.

In order to maintain a well defined spin orientation, the electron transport has to be confined to one dimension. Typical structures for studying one-dimensional transport are quantum wires (Fig. 1). As for the Hall bar samples, quantum wires with a widths down to 600 nm reveal a pronounced beating pattern in the Shubnikov-de Haas oscillations (Fig. 3). This indicates that we are able to preserve the spin precession due to the Rashba effect in quasi one-dimensional structures.

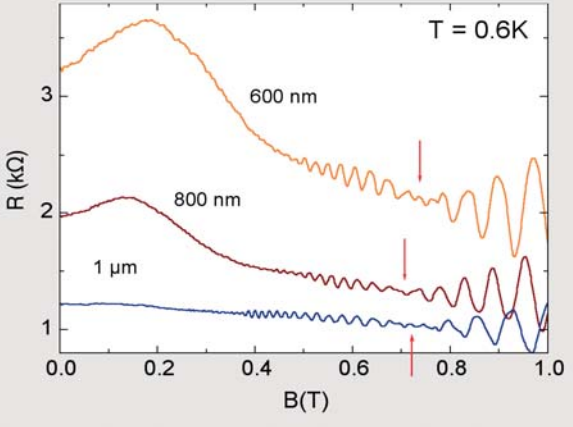

Fig. 3
Magnetoresistance of quantum wire structures of different widths.

As a long term goal the Rashba effect will be studied in the ballistic regime, where no scattering event disturbs the electron propagation. In order to investigate ballistic transport, split-gate point contacts have been fabricated (Fig. 4, inset). Here, the effective channel width between the source and drain contact is adjusted electrostatically by two split-gate fingers. In our samples in-plane split-gates are employed, which are separated from the channel by a trench defined by reactive ion etching. As can be seen in Fig.4, the point contact resistance increases in steps if the channel width is reduced by applying a more negative gate voltage. The steps in the resistance are a clear indication of bal-

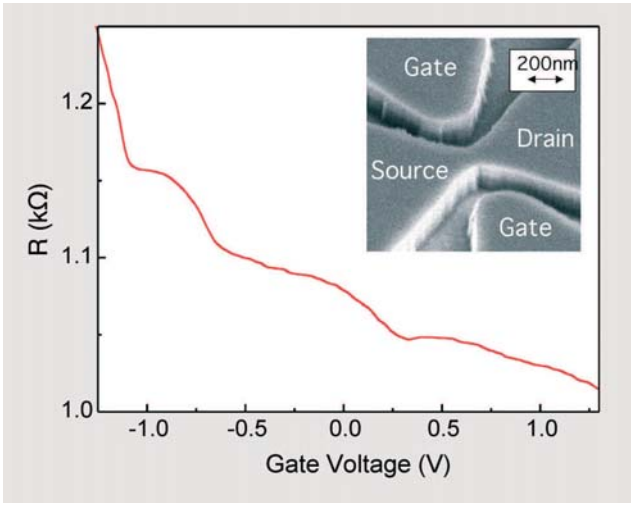

Fig. 4
Resistance of an in-plane gate point contact as a function of the gate voltage. The small picture shows a quantum point contact with in-plane gate electrodes to control the width of the conductive channel between source and drain.

listic transport via one-dimensional subbands which are formed within the point contact constriction. Our present studies are focussed on the magnetotransport of point contact structures in order to obtain more information on the Rashba effect in one-dimensional systems.

REFERENCES

"Effect of the heterointerface on the spin splitting in modulation doped InGaAs/InP quantum wells"
Th. Schäpers, G. Engels, J. Lange, Th. Klocke, M. Hollfelder, and H. Lüth
J. Appl. Phys. **83** (1998) 4324

"Spin-Splitting in InGaAs/InP heterostructures"
Th. Schäpers and H. Lüth
Proc. 10th Int. Conf. on Narrow Gap Semiconductors, Ishikawa, Japan, IPAP Conf. Series 2, (2001) 223

AUTHORS

Hilde Hardtdegen, Andre van der Hart, Jens Knobbe, Thomas Schäpers

Andreev-Reflection in Superconductor/ Semiconductor Structures

INTRODUCTION

In structures with two superconducting electrodes (S), connected by a sufficiently short normal conducting bridge (N), a supercurrent can be observed. In contrast to the well known Josephson elements based on tunnelling through an insulating barrier, here carriers in the normal conductor directly take part in the supercurrent flow between the superconducting electrodes. The appearance of the supercurrent can be explained within the framework of the theory of the Andreev reflection. In an Andreev reflection process an electron in the normal conductor incident on the normal/superconductor interface is retro-reflected as a hole (Fig. 1a). Retro-reflection implies that the hole takes the same path as the incident electron. At the same time a Cooper pair is formed within the superconductor. If two superconducting electrodes are separated by a short normal bridge, Andreev bound states form. They are somewhat similar to bound states in a quantum well (Fig. 1a). These Andreev bound states can carry a current and are responsible for the observed Josephson supercurrent. The total supercurrent in these junctions are determined by the number and the occupation of the Andreev bound states. Very interesting experiments can be performed, if a two-dimensional electron gas (2DEG) in a semiconductor heterostructure is used as the normal conducting layer, because the carrier concentration and thus the supercurrent in a S/2DEG/S junction can be controlled by a gate. Furthermore, the extremely long mean free path in the 2DEG allows experiments in the ballistic transport regime. Besides fundamental studies related to the carrier transport in hybrid structures, Andreev reflections in superconductor/semiconductor structures might also play an important role for the realization of quantum computers.

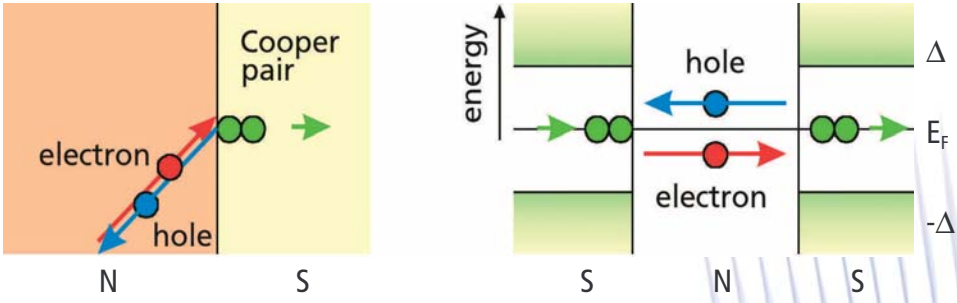

Fig. 1
a) Andreev reflection process in a normal conductor (N)/superconductor (S) structure in real space. The retroreflected hole takes the same path back as the incident electron. In the superconductor a Cooper pair is formed.

b) Energy diagram of the Andreev reflection in a S/N/S junction. At the right interface the electron is retro-reflected as a hole by creating a Cooper pair in the superconductor. At the left interface a hole is retro-reflected as an electron by annihilating a Cooper pair in the left electrode. Here, Δ is the superconducting gap and E_F is the Fermi energy.

APPROACH

We studied the transport properties across junctions between a superconductor and a two-dimensional electron gas (2DEG) [1]. For the superconducting electrodes a thin niobium layer is used. The two-dimensional electron gas is based on a strained InGaAs/InP heterostructure, which provides a low resistance Schottky contact and thus ensures a good coupling between the superconductor and the 2DEG. Due to the high electron mobility of the 2DEG and the small separation of the Nb electrodes (about 500 nm) the carrier transport can be regarded as ballistic, which implies that almost no scattering takes place at low temperatures. The samples are fabricated by electron beam lithography and reactive ion etching in order to define the InGaAs/InP mesa structure. The Nb electrodes are prepared by a second electron beam lithography step and a lift-off process. A typical S/DEG/S structure is shown in Fig. 2. In order to inject carriers into the S/2DEG/S junction, normal contacts are connected to the 2DEG area of the junction.

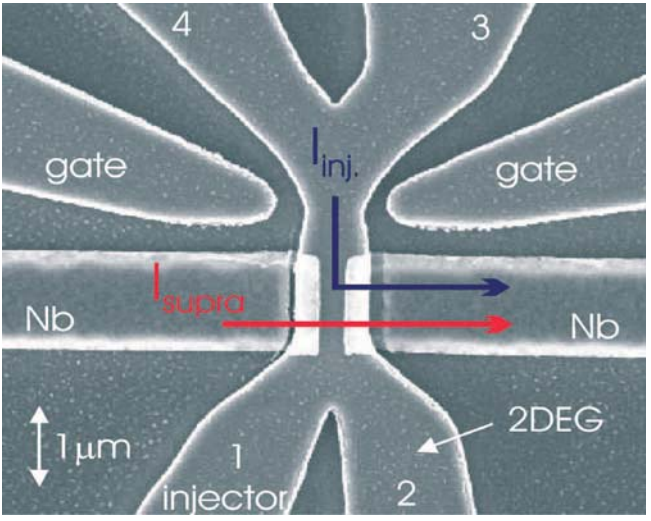

Fig. 2
Scanning electron microscope picture of a superconductor/two-dimensional electron gas/superconductor structure. For the superconducting electrodes Nb was used. The contacts 1 to 4 are used to inject hot carriers into the Nb/2DEG/Nb junction. By biasing the in-plane gate fingers the opening width of the injector can be controlled.

RESULTS

We have prepared superconducting Nb/2DEG/Nb junctions of excellent quality. As can be seen in Fig. 3, a maximum supercurrent of more than 1 µA is obtained for a 6 µm wide junction. A comparison with a theoretical model for a two-dimensional structure confirmed that the supercurrent can be explained by phase-coherent Andreev reflection in the ballistic transport regime. If compared to other types of S/2DEG/S junctions, the large supercurrent across our junctions is a result of our research towards the best superconductor/2DEG interface transparency. By injecting hot carriers via an additional terminal the occupa-

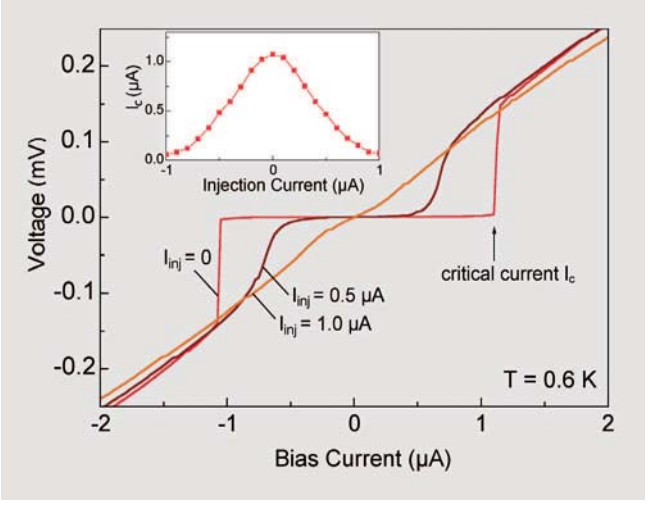

Fig. 3
Control of a Josephson supercurrent by injecting hot carriers into the superconductor/2DEG/superconductor contact via normal conducting electrodes. The inset shows the decrease of the critical current I_c as a function of the injection current.

tion of Andreev levels and thus the net supercurrent can be controlled [2]. This is also shown in Fig. 3. By increasing the injection current, the maximum Josephson supercurrent decreases. This is due to the fact, that formerly unoccupied Andreev bound states become occupied by the injected hot carriers, which carry a supercurrent in the opposite direction. This leads to the observed decrease of the critical current. The influence of the injection current can be resolved with the help of a small external magnetic field [3]. Currently our studies are focussed on the control of the supercurrent by using quantum point contacts as injectors. Furthermore, the Andreev reflection process is investigated under high magnetic fields, where the quantum Hall effect is observed in the two-dimensional electron gas.

REFERENCES

1. "Superconductor/semiconductor junctions"
   Th. Schäpers, Springer Tracts in Modern Physics 174 (2001)

2. "Carrier transport in multi-terminal superconductor/two-dimensional electron gas Josephson junctions"
   V. A. Guzenko, Th. Schäpers, R. P. Müller, A. A. Golubov, A. Brinkman, G. Crecelius, A. Kaluza and H. Lüth, Physica C 352 (2001) 144

3. "Local suppression of Josephson currents in niobium/2DEG/niobium structures by an injection current"
   K. Neurohr, Th. Schäpers, J. Malindretos, S. G. Lachenmann, A. I. Braginski, H. Lüth, M. Behet, G. Borghs, and A. A. Golubov , Phys. Rev. B 59 (1999) 11197

AUTHORS

Igor Batov, Vitaliy Guzenko, Hilde Hardtdegen, Andre van der Hart, Thomas Schäpers

V-Groove Quantum Wires

INTRODUCTION

In recent years several novel approaches have been pursued in order to fabricate quantum wire structures. A very promising technique is the growth on v-shaped patterned substrates. In these v-groove quantum wires energy subband separations of more than 10 meV have been achieved. From a fundamental point of view, v-groove quantum wires can serve as a model system for transport studies on one-dimensional systems with only one conducting channel due to the very good carrier confinement. From a practical point of view, v-groove quantum wires are promising candidates to improve the performance of laser structures, since here very low threshold currents are expected. In addition, quantum wires might also be advantageous for transistor structures due to the reduction of phase space by the additional carrier confinement.

APPROACH

We fabricated AlGaAs/GaAs/AlGaAs quantum wire structures on a GaAs substrate which was pre-patterned with v-shaped grooves. The AlGaAs/GaAs layer system was grown by metal-organic vapor phase epitaxy. A transmission electron microscope cross-section image is shown in Fig. 1(a). The GaAs quantum well layer is embedded in a AlGaAs barrier material. The growth of the GaAs layer results in the formation of a crescent-shaped quantum wire (QWR) at the bottom of the groove, sidewall quantum wells (SQW) and top quantum wells on the (001) surfaces. Inside the AlGaAs barrier spontaneous segregation leads to the evolution of a Ga-rich vertical quantum well (VQW) along the tip of the groove. In Fig. 1(b) a simulation of the first three quantum levels based on a two-dimensional Schrödinger-Poisson solver is shown. From the simulation an energy separation between the first and the second sublevel in the quantum well of more than 10 meV is predicted.

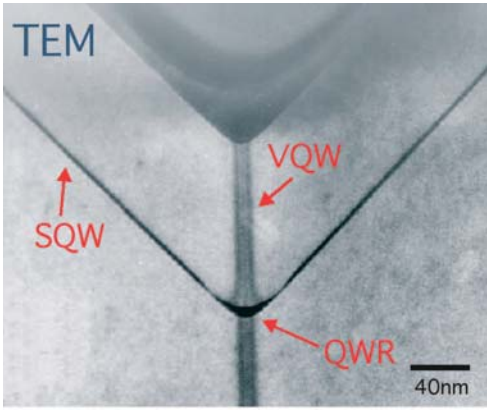

a)

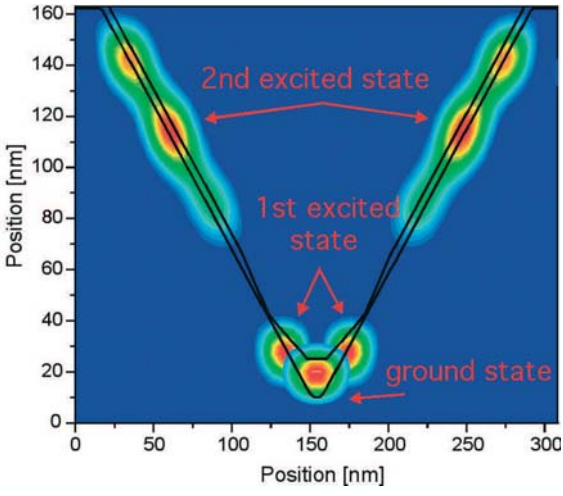

b)

Fig. 1
a) Transmission electron micrograph of a GaAs/AlGaAs v-groove quantum wire (QWR). (TEM picture: D. Meertens, IFF FZ Jülich)
b) Simulation of the first three energy levels.

RESULTS

The quantum wire structures are examined by photoluminescence spectroscopy. A typical spectrum is shown in Fig. 2. The spectrum reveals a number of peaks which can be assigned to different areas of our structure, e.g. the side quantum well, top quantum well or vertical quantum well. Beside these two-dimensional structures, a pair of peaks is found at approximately 1.6 eV, which can be attributed to the crescent-shaped quantum wire. The intensity of these two peaks is lower because of the smaller effective area. By analyzing the energetic distance between the two peaks and comparing them with the theoretically calculated level separation, the predicted large quantization energy is confirmed. By performing scanning near field opti-

Fig. 2
Photoluminescence spectra of a v-groove quantum wire structure.

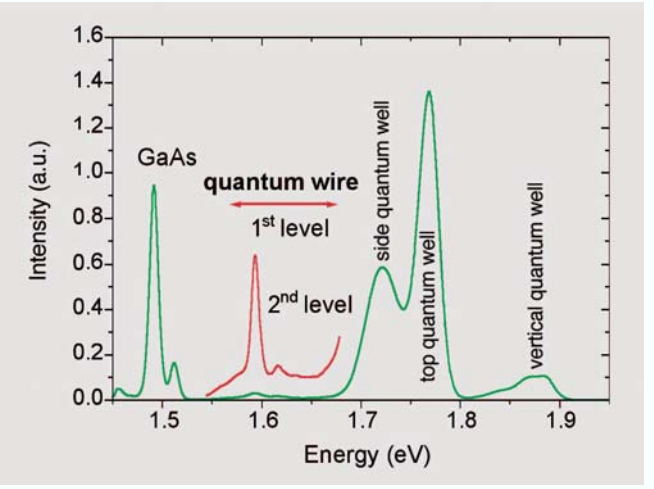

cal microscopy studies (in collaboration with Oxford University) or cathodoluminescence measurements (in collaboration with Magdeburg University) the quantum levels could be visualized directly. By combining optical measurements with carrier transport, information on the carrier relaxation and transfer between the different transport channels were obtained.

REFERENCES

"Electron transport in modulation-doped GaAs V-groove quantum wires"
A. Schwarz, A. Kaluza, H. Hardtdegen, Th. Schäpers, H. Lüth, D. Meertens, Ch. Dieker, A. C. Maciel, J. Kim, E. D. O'Sullivan, and J. F. Ryan,
Physica E 7 (2000) 760

"On the choice of precursors for the MOVPE-growth of high-quality AlGaAs/GaAs v-groove quantum wires with large sub-band spacing"
A. Kaluza, A. Schwarz, D. Gauer, H. Hardtdegen, N. Nastase, H. Lüth, Th. Schäpers, D. Meertens, A. C. Maciel, J. F. Ryan, and E. D. O'Sullivan,
J. Cryst. Growth. 221, 91-97 (2000)

AUTHORS

Torsten Bronger, Hilde Hardtdegen, Andreas Kaluza, Jens Knobbe, Thomas Schäpers, Axel Schwarz

Luminescence of Nanoscale Ge Islands on Si(110) and Si(001)

INTRODUCTION

The simultaneous growth of germanium islands on different silicon surfaces has shown significant differences in the self-assembling on Si(110) and Si(001). There are both fundamental and technological advantages associated with growth on Si(110). Ge quantum dots on Si(110) are predicted to have stronger electron confinement due to a larger conduction band-offset compared to Ge/Si(001). Furthermore, the existence of a {111} cleavage plane perpendicular to the (110) surface is interesting for coupling light into optical waveguides.

The (001) and (110) surfaces differ by their atomic density, surface energy, surface reconstruction and their incorporation probability. The (110) surface is a high symmetry, low index surface. Atoms on {110} surfaces are arranged in zigzag chains, each surface atom having one unsatisfied bond. The first deposited atom to start the formation of a new layer makes only one bond to the existing surface creating three dangling bonds. A second atom is needed to bond the first adatom to the underlying surface. This makes incorporation difficult, resulting in a low growth rate, in contrast to (001) where the two dangling bonds available are responsible for the highest growth rate [1]. The clean surface has a (16x2) reconstruction up to 760°C, with 2.5 nm broad terraces with a height of one monolayer and edges parallel to <112> directions [2]. The (110) surface is more dense (surface density 1.4 times larger than for the (001) surface) and has a larger Young modulus. One monolayer is 0.19 nm high (0.138 nm on Si(001)).
Here, the morphology and the electrooptical properties of Ge islands grown at 700°C on Si(110) were studied in comparison with growth on Si(001).

Si(001) #1677

Si(110) #1679

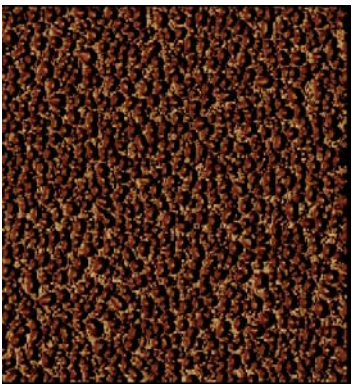

Fig. 1
AFM images of uncapped Ge islands on Si(001) and Si(110) with nearly the same thickness (~ 1.8 nm), height (~28 nm) and width (~123 nm); scan size 5x5 μm^2

Experimental

Growth was performed at 0.12 Torr and 700°C in a LPCVD system with a base pressure of $6x10^{-8}$ Torr. Si(110) substrates were RCA cleaned before loaded into the LPCVD system [3]. The Si source is $SiCl_2H_2$ and the Ge source GeH_4 diluted in He. AFM studies were performed on uncapped samples, for electroluminescence (EL) studies Ge was capped with Si or SiGe. The nominal Ge coverage was in the range 0.3 – 2 nm.

Island Morphology

We observed the 2D to 3D transition to occur at ~ 4 monolayers on both surfaces [3]. For (110) this corresponds to a thicker Ge layer of ~ 0.8 nm (0.57 nm on Si(001)). This agrees well with the estimation of the critical wavelength, λ_0 of the Asaro-Tiller-Grinfel'd instability responsible for the islands formation with $\lambda_0 \sim \gamma E/s^2$, where γ - surface energy, E – Young modulus, σ - strain. Both g and E are larger for the (110) surface, while σ is smaller. This leads to a longer wavelength, i.e. island formation starts for a thicker layer on Si(110).

The evolution of island density and size during growth is mainly governed by the elastic interation between islands. The large island density (45 μm^{-2} as compared to 16 μm^{-2} on Si(001) see Fig.1) corresponds to a small inter-island distance. The elastic interaction between islands can reduce the critical volume for the pyramid to dome transition, therefore the island-island interaction might be responsible for the nucleation of only domes just after the 2D to 3D transition.

As all growth experiments were performed at 700°C interdiffusion is expected to be strong. One feature of Fig.1 is that the higher density of islands on the (110) with nearly the same sizes on both surfaces can only be explained by a stronger interdiffusion on Si(110) in agreement with the photoluminescence studies.

Capping effects

We have observed that capping leads to a loss of Ge from the islands on Si(110), but not from islands on Si(001). This is illustrated in Fig.2 by the much smaller islands on the (110) surface. The thinner cap layer on the (110) sample is due to the lower growth rate on (110) surfaces. On Si(110) the island height is reduced from 27 nm to 2-7 nm, the island width is reduced from 120 to 35 – 80 nm.

The island density is also reduced by 30% due to the dissolution of smaller islands. The mechanism responsible for this phenomenon is the etching reaction Ge + 4HCl -> $GeCl_4$ which occurs during the growth of the first monolayers of the Si cap layer. HCl is the reaction product during the Si growth by $SiCl_2H_2$. This reaction is favoured on the Si(110) surface due to the much lower growth rate. Deposition of Si with a higher rate, for example using SiH_4, should help to avoid the etching reaction.

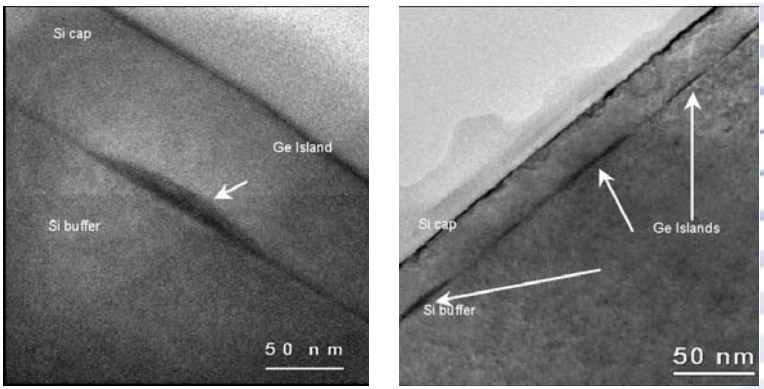

Fig. 2
Cross-section TEM of capped Ge islands on (001) and (110) Si substrates. The Si cap layer on (001) is thicker due to the higher growth rate, the island height on (110) is smaller due to the etching reaction.

Electroluminescence

For the study light emitting PIN diodes with islands capped with boron-doped SiGe were realized. Fig. 3 shows EL spectra of selectively grown diodes of 1mm^2 area deposited on n$^+$Si(110) and n$^+$Si(001) in one run. Due to the etching effect during capping the island morphology in the two samples is quite different. In the (001) diode the distribution is bimodal, 10 - 20 nm high with 10 islands/μm^2. In the (110) diode islands are monomodal, 2-7 nm high and of higher density ~ 30μm^{-2}. These features are well reflected in the EL. While the EL of the (001) diode reveals two contributions with different temperature and injection behaviour, the emission of the (110) diode is due to only one kind of islands and has an intensity three timnes higher. The peak position of the (110) diode shifts to higher energy with

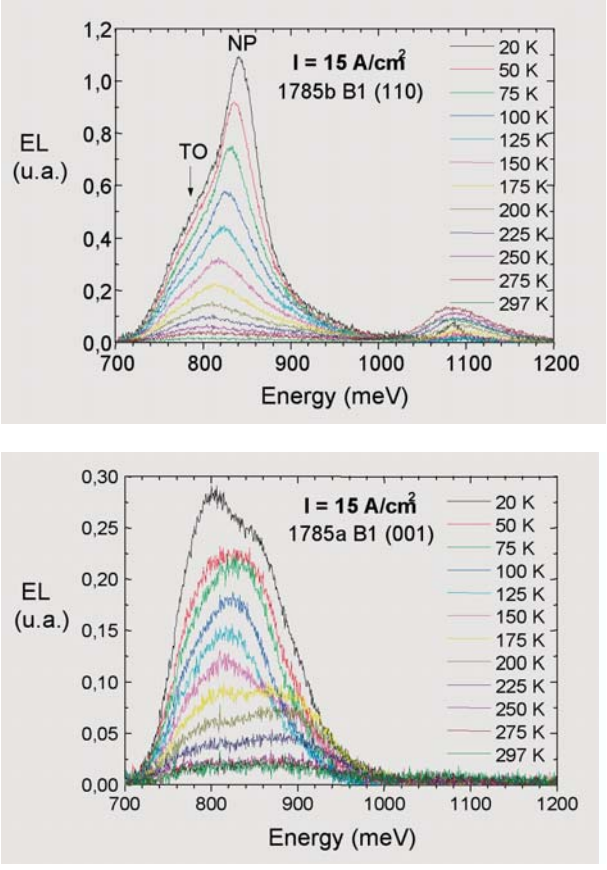

Fig. 3
Temperature dependence of EL of diodes with an area 1000x1000 μm^2 of epitaxy No.1785:
(a) on Si(110) and (b) on Si(001). The scale of the ordinate for both graphs is identical.

current due to the carrier filling effect. The peak position of the (110) diodes lies at lower energy and nearer to $\lambda = 1.55\mu m$, although the Si content is higher and the islands are much shallower.

SUMMARY

The morphology of islands on Si(110) shows a dense, monomodal distribution of elongated domes with a stronger interdiffusion than on Si(001) for the studied high growth rates and short deposition times. The light emission is close to 1.55 μm with an emission intensity three times higher than on Si(001) up to room temperature. This is mainly due to the larger areal density of the islands.

REFERENCES

[1] L. Vescan, K. Grimm and C. Dieker,
J. Vac. Sci. and Techn. B16 (1998) 1549

[2] R. Butz and H. Lüth,
Surf. Sci. 365 (1996) 807

[3] P. Ferrandis,
PhD thesis, 2002, INSA, Lyon, France

AUTHORS

Lili Vescan, Philipp Ferrandis and Toma Stoica

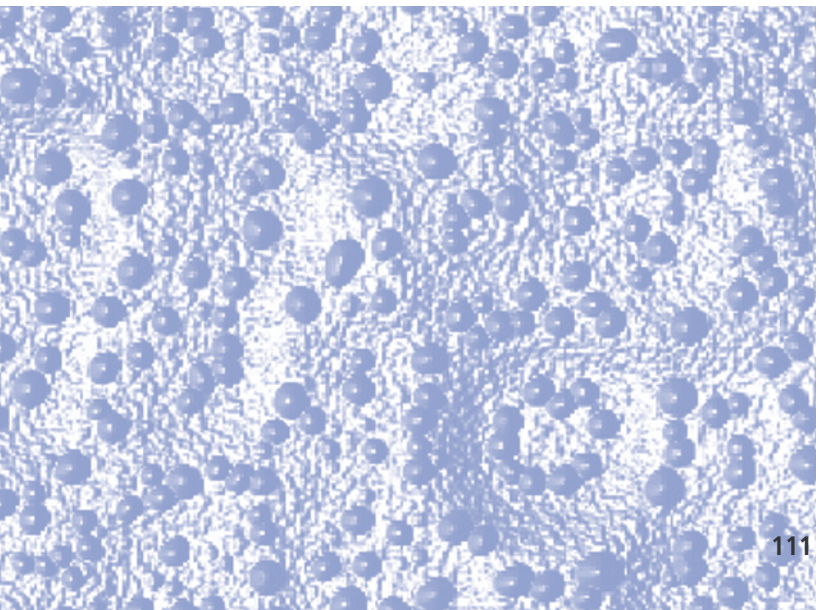

Generation of Terahertz Radiation by Frequency Mixing in Low Temperature GaAs

INTRODUCTION

It is well known that GaAs grown by molecular-beam epitaxy at low temperatures **(LT GaAs)** exhibits high specific resistivity (>10^6 Ω cm) and a high electric breakdown strength (~300 kV/cm) as well as a short carrier lifetime (~0.3 ps). These parameters allow the preparation of high-speed and high-voltage photoconductive switches and detectors. Moreover, LT GaAs photodetectors can serve as tunable sources of terahertz radiation by using photonic mixing, which generates a signal at a difference frequency.

LT GaAs contains a considerable excess of arsenic (up to 1.5 at. %), which is accommodated in the lattice in the form of various native defects. They form electronic traps. The concentration of deep traps depends on the growth temperature and post-growth thermal treatment. This allows an adjustment of the electrical and optical properties of LT GaAs. However, detailed role of the traps is not yet fully understood. Therefore the influence of the material properties on the device performance needs to be studied in detail. Recently we investigated basic properties of LT GaAs layers and photodetectors. Presently studies concerning the LT GaAs photomixers as sources of terahertz radiation are performed in a co-operation with the Max-Planck-Institut für Radioastronomie Bonn and Universität Köln (SFB 494).

APPROACH

The LT GaAs layers were grown on semi-insulating GaAs at a substrate temperature of 200-400 °C by the MBE technique. A 300nm thin AlAs interlayer was inserted to separate the layer from its substrate by selective etching lift-off technique [1]. This permits transport measurements without any contribution of the substrate to the conductivity. Twelve double layers of AlAs/GaAs were inserted between the substrate and the

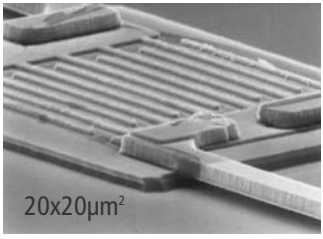

Fig. 1
LT GaAs photodetector with interdigitated finger contacts.

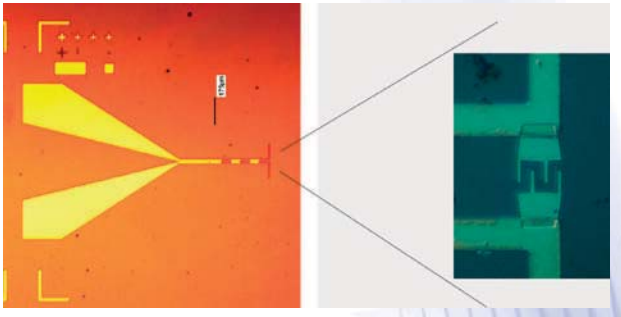

Fig. 2
LT GaAs photomixer chip with interdigitated MSM structure and planar single-dipole antenna for 460 GHz.

undoped LT GaAs layer to create a resonant cavity in order to improve the light absorption efficiency for the photomixer. Most samples were annealed in-situ for 10 min at 600 °C. Metal-semiconductor-metal (MSM) photodetectors were prepared by conventional device processing steps as optical or e-beam lithography, metal evaporation and lift-off (Fig. 1). Samples with various geometries of the interdigitated finger contacts were used. The finger spacing and width was in the range of 1-2 µm and 0.2-0.5 µm, respectively. The complete photomixer includes an integrated photodetector, a planar single-dipole antenna as well as a coplanar strip line and bonding pads (Fig. 2).

RESULTS

Transport properties

The concentration of deep traps in LT GaAs can be as high as 10^{19}-10^{20} cm^{-3} and the transport of carriers can be described by a combination of band conduction and a hopping contribution [1]. This explains the observed anomalous temperature dependence of the carrier concentration in LT GaAs, as shown in Fig. 3. In the temperature range of interest the conductivity changes from hopping conduction (sample grown at 250 °C) to band conduction (400 °C growth temperature). Samples grown at intermediate temperatures (300-350 °C) exhibit a combined conduction. In this case the carrier concentration can decrease with increasing temperature.

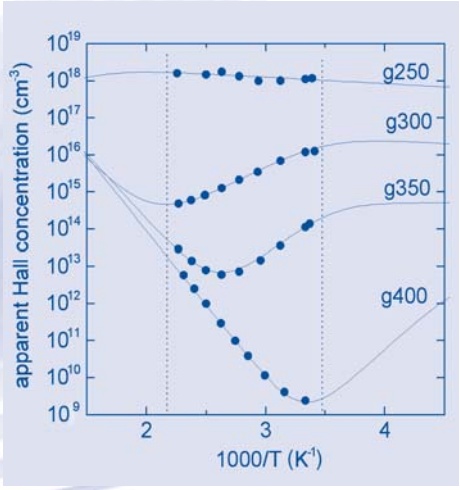

Fig. 3
Hall concentration vs. inverse measurement temperature for LT GaAs grown at different temperatures (250 °C – 400 °C). Full lines are calculated considering combined band and hopping conduction [1].

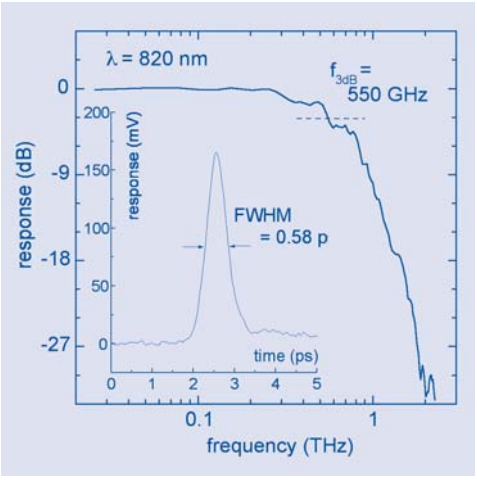

Fig. 4
Fourier transform of the response of LT GaAs photodetector and measured time resolved response (inset) [2].

Ultrafast photodetectors

We have fabricated MSM photodetectors on LT GaAs (Fig. 1) and demonstrated that a bandwidth of 550 GHz can be achieved by such devices [2]. In a first series of experiments the lifetime of photogenerated carriers was studied using time-resolved reflectivity (TRR) measurements. The annealed samples grown at 200 °C show an extremely fast reflectivity decay and a carrier lifetime of 0.2 ps was measured. The transient behavior of the LT GaAs photodetectors was studied by measurements of the photoresponse after a femtosecond excitation pulse. The observed signal was nearly symmetric with an FWHM of 0.6 ps (inset in Fig. 4). To our knowledge, this is the fastest response of a semiconductor photodetector.

Fig. 4 shows the frequency response of LT GaAs photodetector obtained by Fourier transforming the detected pulse. The observed bandwidth amounts to 550 GHz, which is higher than ever reported. From the measured carrier lifetime, the microwave capacitance and the 75 Ω transmission line impedance it fol-

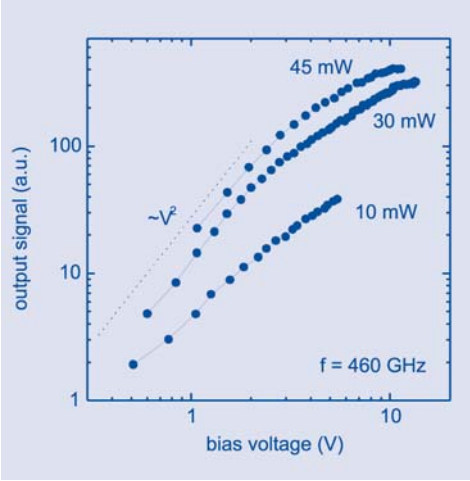

Fig. 5
460 GHz output power of LT GaAs photomixer as a function of bias voltage for three different optical input powers [3].

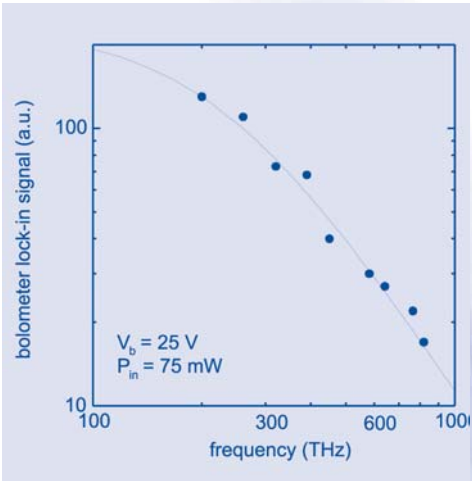

Fig. 6
Output power of LT GaAs photomixer as a function of frequency [measurement by E. Michael, Uni Köln, unpublished].

lows that the bandwidth of the studied devices is limited by the RC time constant. Further improvements can be expected by reducing the detector area, thereby lowering the device capacitance.

Photomixers

Two types of photomixers on LT GaAs have been developed. The first consists of an 5x8 μm^2 MSM detector integrated with a single-dipole antenna and a coplanar strip line (Fig. 2). These devices are designed to generate radiation at 460 GHz [3]. Fig. 5 shows the output power as a function of the bias voltage at three different input powers. An output power level of ~1 µW can be obtained at 460 GHz. The output power P_{out} at a lower bias V_b follows the $P_{out} \cong V_b^2$ dependence, according to the theory. However, at a higher bias and higher input powers a saturation of P_{out} is observed. This effect is attributed to heating effects, as the input power density reaches values of ~100 kW/cm^2. The thermal management of the photomixer needs to be improved

before any further increase of the radiated output power. We also developed photomixers based on the traveling-wave geometry. They consist of LT GaAs, on which a coplanar strip line with 2 µm gap and a broadband bowtie antenna are integrated. First results on this type of LT GaAs photomixer show that it is possible to detect radiation up to 810 GHz, using an InSb bolometer (75 mW input power, 25 V bias voltage, see Fig. 6). The measured data follow the theoretical P_{out} vs. frequency dependence with two time constants (RC and τ_e, full line in Fig. 6). The data suggest, that the output power can be further improved.

REFERENCES

[1] "On the hopping and band conductivity in molecular-beam epitaxial low-temperature grown GaAs"
M. Morvic, J. Betko, J. Novák, A. Förster, and P. Kordoš
Phys. Stat. Solidi (b) 205, 125 (1998)

[2] "550 GHz bandwidth photodetector on low-temperature grown molecular-beam epitaxial GaAs"
P. Kordoš, A. Förster, M. Marso, and F. Rüders
Electron. Lett. 34, 119 (1998)

[3] "Generation of 460 GHz radiation by photomixing in low-temperature-grown MBE GaAs"
M. Mikulics, F. Siebe, A. Fox, M. Marso, A. Förster, H. Stüer, F. Schäfer, R. Güsten, and P. Kordoš
Proc. 4th Intern. Confer. Advanced Semicond. Devices and Microsystems, ISBN: 0-7803-7276-X, p. 129 (2002)

AUTHORS

Martin Mikulics, Arno Förster, Michel Marso and Peter Kordoš

A Vertical Resonant Tunneling Transistor (VRTT) for Digital Electronics

INTRODUCTION

Two main factors will limit the rapid increase in device density of highly integrated microelectronic circuits:

- the smallest dimension that can be defined by optical lithography and
- the so-called quantum limit.

Although the improvement in classical processing techniques does not seem to reach these limits as fast as predicted, the quantum limit will be reached probably in the next decade. Presently this limit seems to be the most fundamental restriction. This does not necessarily stop the progress in microelectronics, but it will turn the attention of the researchers to new ways and new ideas. In this sense, the progress in the development of resonant tunneling diodes (RTDs) [1] represents one example in the field of quantum transport devices at room temperature. On the one hand, RTDs are ideal model-structures for fundamental research studies of quantum phenomena, like Coulomb blockade in quantum dots [2,3]. On the other hand, RTDs have demonstrated a strong potential for future digital electronics [4]. Compared to conventional devices RTDs offer the advantage of high speed of operation, low power dissipation and low circuit complexity due to higher functionality.

The thorough investigation of quantum transport phenomena and advances in epitaxial-growth technology have significantly improved the performance of resonant tunneling diodes. Particularly the substantial progress in the manufacturability of RTD devices in the past years is important for the realization of RTD circuits [5]. Their current-voltage characteristics exhibits a region of negative differential resistance (NDR) as the macroscopic manifestation of the quantum mechanical tunneling effect, which can be observed clearly even at room temperature (Fig. 1).

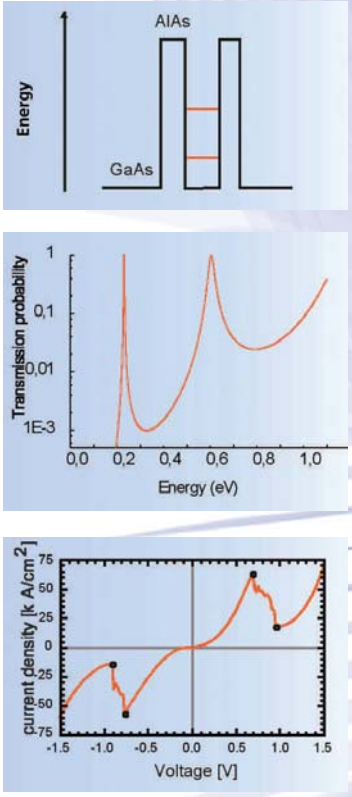

Fig. 1
Main features of a Resonant Tunneling Diode (RTD)
a) Band structure
b) Transmission probability
c) I-V curve

Many applications that exploit this negative differential resistance feature have been proposed in the last years and various promising RTD-based logic elements and high frequency devices have been demonstrated.

APPROACH

Most of the RTD applications make use of the MOBILE operation principle that is described in detail below. This logic gate employs a monostable-to-bistable transition of a circuit that consists of two RTDs connected in series. A small difference between the peak currents of the RTDs determines the state of the circuit after the transition. There are different approaches to control the RTDs peak current. On the one hand conventional transistors can be integrated into the circuit and on the other hand three-terminal resonant tunneling devices manipulating the peak current by means of an Schottky gate or a p-n-junction have been fabricated. The concept of a three-terminal resonant tunneling device has significant advantages over the integration of RTDs and conventional transistors like HFETs (heterostructure field effect transistors). The HFET and RTD characteristics have to match each other, for instance the transistor current and the RTD peak current. Thus, the transistors have to be fabricated with very little tolerance of the device properties, whereas in a three-terminal resonant tunneling device the matching between RTD and FET is inherently fulfilled. Furthermore this concept offers the advantage of lower complexity. The VRTT device consists of a small square mesa diode surrounded by a Schottky type depletion gate which is structured in a self-aligned evaporation process. The peak current will be controlled by the voltage dependent thickness of the space charge layer.

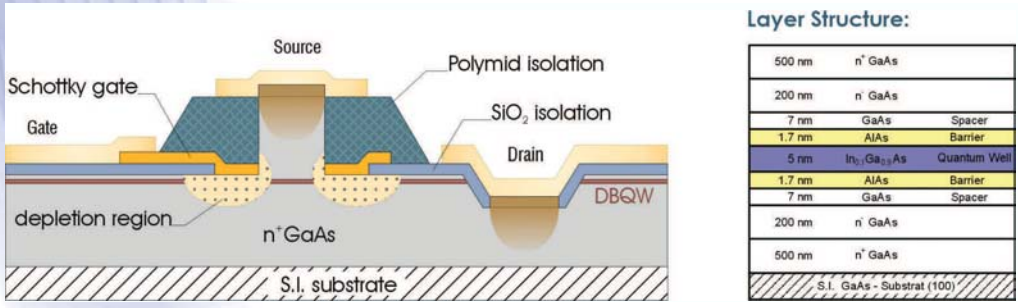

Fig. 2
Scheme of a vertical resonant tunneling transistor (left) and the corresponding layer structure (right).

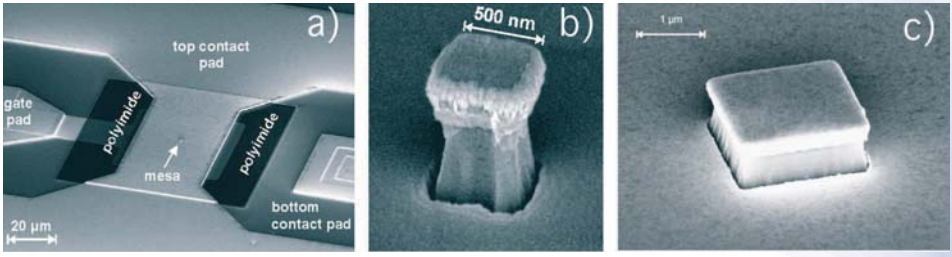

Fig. 3
Scanning electron micrographs:
a) completely processed resonant tunneling transistor,
b) 500 nm mesa,
c) 2µm mesa

Fig. 2 shows a schematic view of the device. Fig. 3 shows a scanning electron micrograph of the completely processed device with different mesa sizes.

The epitaxial structure used to fabricate the VRTT device was grown by molecular beam epitaxy (MBE) on semi-insulating (100)-orientated GaAs substrate (Fig. 2). The layer structure can be subdivided into the actual RTD layer structure and two adjacent electron reservoirs. Low-doped n-GaAs layers are introduced to achieve enhanced control of the device current.

Two vertical resonant tunneling transistors (VRTTs) connected in series (Fig. 4) are the basis for a MOBILE (Monostable-bistable transition logic element). A small difference between the peak currents of the VRTTs determines the state of the circuit after the transition. As long as the clock voltage is less than twice the peak voltage there is only one stable point (A in Fig. 5a). If the clock voltage exceeds the double peak voltage this stable point splits into two stable points (B and C in Fig. 5b and 5c, respectively) representing the two logic states of the MOBILE. After this monostable-to-bistable transition the state of the circuit is determined by a small difference in the peak currents of the load and the drive VRTT. If the peak current of the drive VRTT is smaller than the peak current of the load VRTT the circuit switches to the stable point B corresponding to a high output voltage (Fig. 5b). A greater peak current in the drive VRTT results in the stable point C with low output voltage (Fig. 5c). Thus, the state of the circuit is determined by the magnitude of the peak current of the drive VRTT.

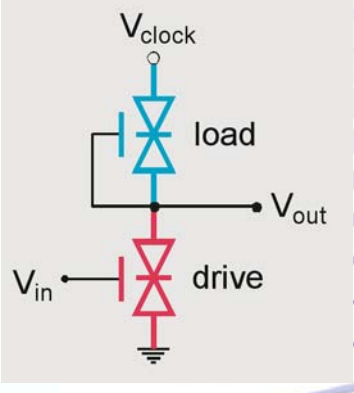

Fig. 4
MOBILE circuit with two VRTTs

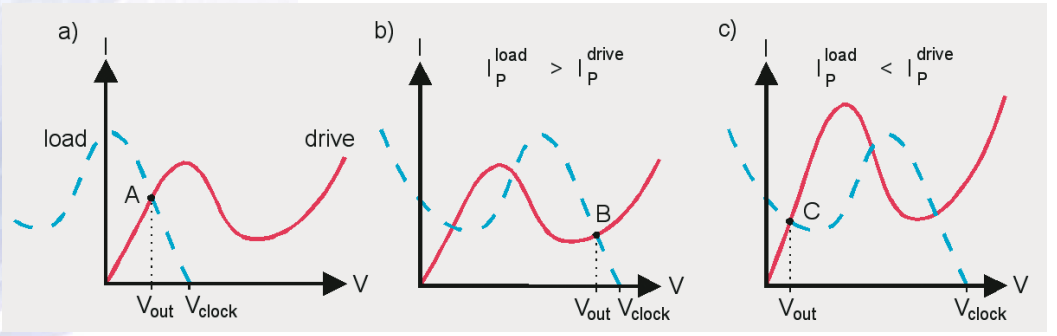

Fig. 5
MOBILE operation scheme a) – c) realized with two VRTTs in series (Fig. 4)

RESULTS

Although the VRTT device is based on a completely symmetric layer structure the current-voltage characteristics exhibits an asymmetric behavior with respect to the bias voltage polarity. We have shown that these effects are related to the asymmetric geometry of the device itself. In the configuration, in which the bottom contact is grounded, the mesa channel is more and more depleted with rising bias voltage and thus, the effective cross section of the mesa decreases. This leads to the observed saturation in the drain current (Fig. 6a). If the top contact is grounded the mesa channel is less depleted with rising bias voltage (Fig. 6b). Thus, the effective cross section of the mesa increases and the drain current rises without saturation.

Concerning a possible application in digital switching units the current-voltage characteristics in Fig. 6b deserves special attention, as it exhibits the behavior of a RTD with controllable peak current I_P. Gate voltages in the range from U_{GS}= +0.2 V to

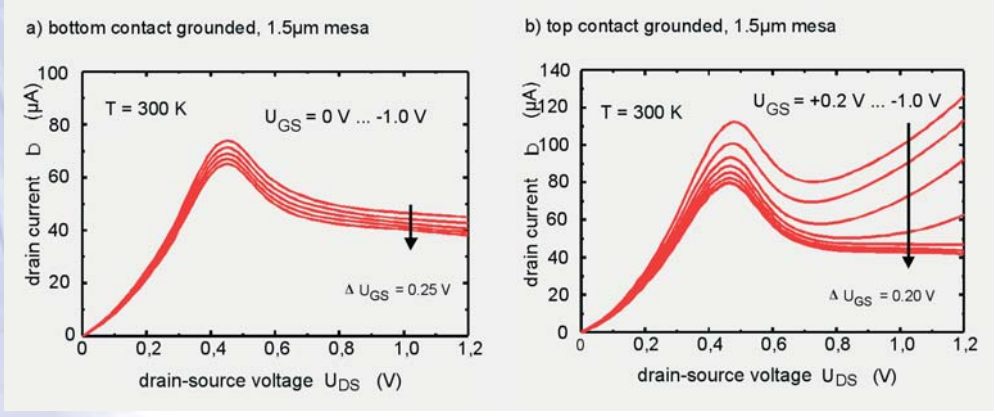

Fig. 6
Current-voltage characteristics of the VRTT device for different bias voltage configurations. a) bottom contact is grounded, the gate voltage is varied from 0 V to -1.0 V in steps of 0.25 V, b) top contact is grounded, the gate voltage is varied from +0.2 V to -1.0 V in steps of 0.2V

U_{GS}= -1.0 V have been applied. Thus, also positive gate voltages can be used to control the peak current. The corresponding gate leakage current was less than 3 nA and hence five orders of magnitude lower than the measured drain current. In the specific range of gate voltages the peak current could be reduced from I_P=112 µA at U_{GS}=+0.2 V to I_P=80 µA at U_{GS}=-1.0 V. The peak voltage of U_P=0.47 V scarcely depends on the applied gate voltage. Peak-to-valley ratios between 1.4 and 2 with a peak current density of 6600 A/cm2 were obtained. In summary the gate voltage can control the peak current efficiently. Thus, the device is suitable for digital switching units operating at room temperature.

The operation of a self latching inverter circuit based on the MOBILE principle was tested. Two VRTTs with square mesas of 2 µm edge length were used and the circuit (Fig. 4) was driven by a clock voltage of V_{clock} = 1.2 V. A gate voltage was applied to the drive VRTT in order to induce the output voltage transition. Fig. 7b shows the measured switching characteristics (output voltage versus clock voltage) of the MOBILE for gate voltages in the range from V_{gate} = +0.3 V to V_{gate} = -0.3 V. When the clock voltage reaches 2_{VP} = 0.9 V the MOBILE switches either to the high or to the low state depending on the applied gate voltage. The output voltage in Fig. 2b exhibits a very sharp transition between the two output states around V_{gate} = 0 V. Only a slight variation in the gate voltage results in a large change of the output voltage. Finally, when the clock voltage has reached its maximum of 1.2 V the output voltage is approximately 0.3 V in

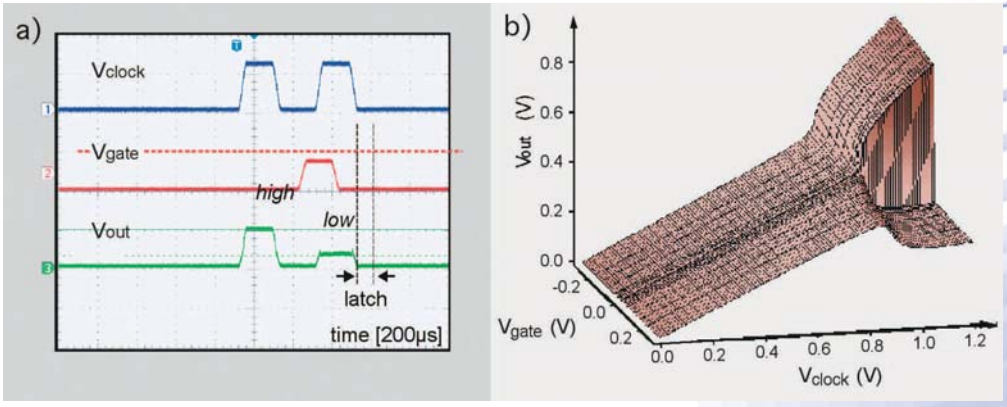

Fig. 7
Low frequency self latching inverter build up with two vertical resonant tunneling transistors in series: a) pulse mode, b) DC mode

the low state and 0.9 V in the high state. Fig.7a demonstrates the inverter operation of the MOBILE circuit using pulsed gate and clock voltages. The traces show the clock voltage, the gate voltage and the output voltage from top to bottom. The output switches to the high level if the input voltage is low and it switches to the low level if the input voltage is high. Note that the output voltage remains constant until the clock voltage returns to zero, although the gate voltage has already changed. This self latching characteristic is an important requirement in digital circuit applications.

In conclusion we have shown that a unit of two VRTT in series can be used as a very sensitive MOBILE. It could be used as extreme fast and versatile element in digital applications.

REFERENCES

[1] A. Förster, Resonant Tunnelig Diodes: The effect of structural properties on their performance, Vieweg, Braunschweig/Wiesbaden ed. by R. Helbig, 1992, pp. 37-62, Festkörperprobleme, Advances in solid state physics, 33rd edition

[2] A. Förster, H. Lüth and Th. Schäpers, Spektrum der Wissenschaften Juni 1999, 88 (1999)

[3] K. M. Indlekofer, A. Förster, H. Lüth, Physica B, 314, 499 (2002)

[4] Koichi Maezawa and Arno Förster, Quantum Transport Devices based on Resonant Tunneling, Nanoelectronics and Information Technology, (2003), ed. R. Waser, Wiley VCH Verlag, Weinheim, Germany

[5] J. Malindretos, A. Förster, K. M. Indlekofer, M. I. Lepsa, H. Hardtdegen, R. Schmidt and H. Lüth, Superlattices and Microstructures 31, 315,(2002)

AUTHORS

Arno Förster, Jürgen Stock, Klaus Michael Indlekofer, Jörg Malindretos, Hans Lüth

The Quantum Transport Simulation Program "WinGreen"

INTRODUCTION

The design of novel semiconductor device structures and the exploration of promising new material systems such as Nitride-based III/V compound semiconductors requires sophisticated simulation tools. Furthermore, considering nano-scale device concepts, the incorporation of quantum phenomena such as tunneling or quasi-bound states is impossible without a physical model based on quantum kinetics. In order to fill this gap, we have developed the simulation package called "WinGreen", providing a fully-featured graphical user interface which offers a high level of comfort during the design stage, simulation stage and finally the evaluation of a new device structure.
The simulation kernel of WinGreen is based on a Green`s functions approach in order to describe non-equilibrium states of a system in the quasi-ballistic quantum transport regime. Supported material systems include AlAs/GaAs, InAlAs/InGaAs/InP, and AlN/InN/GaN. Furthermore, multi-band extensions of the program have been implemented recently. WinGreen is able to run on a variety of Microsoft Windows-based operating systems and is freely available for download on the WWW for non-commercial purposes [1].

APPROACH

Real-time Green's functions represent a quantum mechanical approach for the description of dynamical and kinetic properties of interacting many-particle systems [1-3]. They describe time-space quantum correlations in a general thermodynamical non-equilibrium state and are the first-principles starting point for the incorporation of interaction and scattering, including full bandstructure details with multiple bands and valleys.
WinGreen is physically based on an empirical tight-binding real-time Green`s functions approach in order to describe non-equilibrium states of the system during a transport situation. Device

structures are defined on the basis of spatially localized monoatomic layers, which provides the most accurate way to describe a layered heterostructure. Here, the considered semiconductor device is coupled to two electronic reservoirs each in thermal equilibrium with a given chemical potential. Scattering within the reservoirs is incorporated by means of an optical potential. Furthermore, interaction between free carriers, charged impurities and interface polarization charges is taken into account within the scope of a Hartree-selfconsistent potential. For varying external bias voltages the program is capable of calculating the particle current density, transmission probability in the device region, local charge density, potential profile, local density of states and the energetic injection spectrum of electrons originating from reservoirs.

RESULTS

As an example of a quantum transport device, we discuss the 1-band simulation of a AlAs/GaAs resonant tunnelling diode (RTD) layer structure as shown in Fig. 1, exhibiting the typical double-barrier layer structure.

The following figures visualize some examples of physical information which can be obtained from the WinGreen data output, such as the local density of states (Fig. 2) and the IV characteristics (Fig. 3). For more details can be found in Ref. 1 and 2.

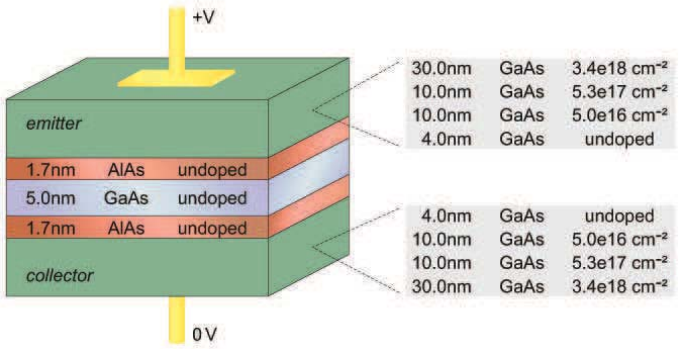

Fig. 1
RTD layer structure with AlAs double-barriers and a GaAs quantum well. Highly n-doped layers built the reservoir regions (contacts).

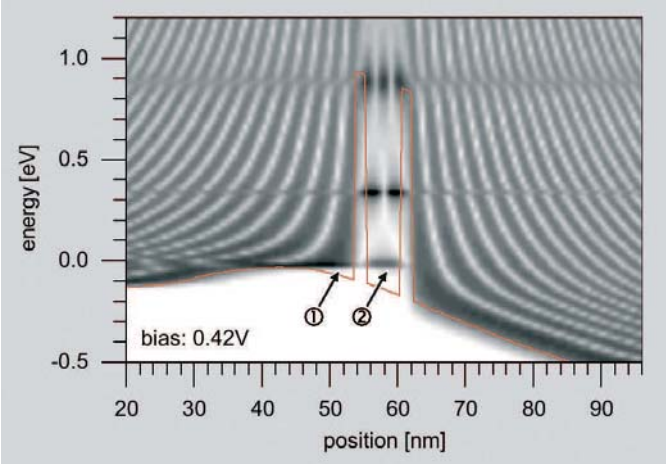

Fig. 2
Local density of states. The selfconsistent potential profile is also drawn for clarity. Point 1 denotes an emitter well quasi-bound state and Point 2 the lowest resonance (quasi-bound state) inside the RTD quantum well.

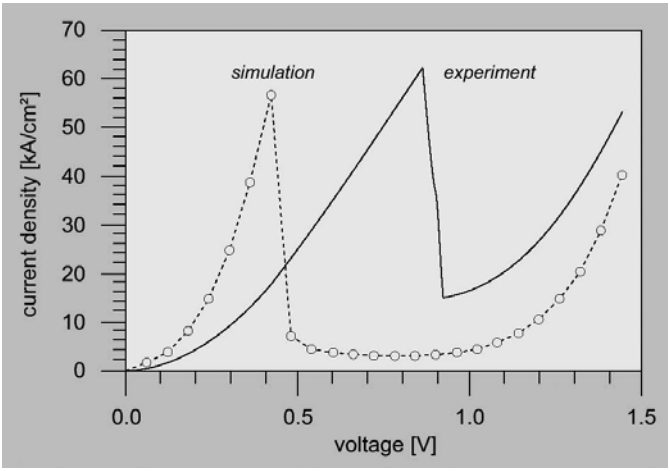

Fig. 3
Simulated IV-characteristics with the typical region of negative differential resistance due to a reso-nance within - the quantum well. The series resistance has not been accounted for in the simulation.

REFERENCES

[1] K. M. Indlekofer, J. Malindretos:
http://www.fz-juelich.de/isg/mbe/wingreen.html

[2] K. M. Indlekofer,
Berichte des Forschungszentrums Jülich, Jül-3705 (1999)

[3] R. Lake, G. Klimeck, R. C. Bowen, D. Jovanovic,
J. Appl. Phys. 81, 7845 (1997)

AUTHORS

Klaus Michael Indlekofer, Jörg Malindretos

AlGaN/GaN HEMTs on Sapphire and Silicon Substrates

INTRODUCTION

AlGaN/GaN high electron mobility transistors (HEMTs) are suitable candidates for high power, high frequency and high temperature electronics (Fig. 1). Progress in the growth and process technology has recently led to the demonstration of very impressive results for the output current density, gain cutoff frequencies and the output power density of AlGaN/GaN HEMTs. However, various problems related to the material structure (high density of defects and traps) as well as the device performance (dc / rf dispersion, channel self-heating, etc.) still need to be solved. Sapphire and since recently also SiC are used as substrates because of the lack of large-area GaN bulk crystals. Silicon wafers are a useful alternative because of the low cost, the large size, good thermal conductivity and the potential to integrate GaN power devices with Si electronics. Here we compare the electrical dc and rf properties of AlGaN/GaN HEMTs on sapphire and silicon substrates, paying special attention to power applications.

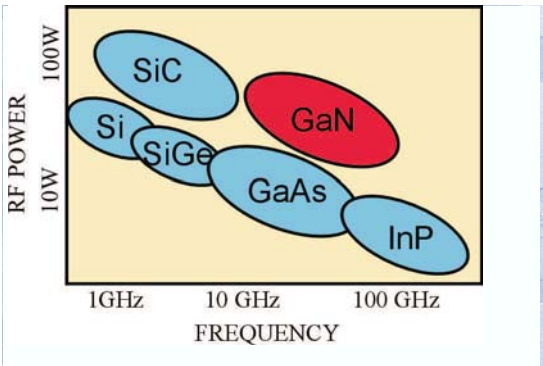

Fig. 1
Regime of operation of GaN and competitive semiconductor materials

APPROACH

The low-pressure MOVPE technique is used to grow AlGaN/GaN heterostructures on (111) silicon, and for comparison on 2 inch c-plane sapphire substrates. This is done at AIXTRON AG, Aachen. A low-temperature nucleation layer is grown first, followed by a GaN buffer layer. Finally, an undoped AlGaN spacer, a Si-doped AlGaN carrier-supply and an undoped AlGaN barrier layer are grown. In the case of structures on Si substrate a special layer series is grown prior to the GaN buffer. Crack-free structures with reduced tensile strain and very smooth surfaces are obtained [1].

The device processing consists of conventional AlGaN/GaN HEMT fabrication steps. It starts with a 200 nm deep mesa etching, enough to completely remove the two dimensional electron gas at the GaN/AlGaN heterojunction. Ohmic contacts are prepared with Ti/Al/Ni/Au followed by an annealing step at 900°C. The Schottky gate metallization consists of a Ni/Au layer patterned by e-beam lithography. Unpassivated two-, four-, and six-finger devices with different source-drain separation were prepared. The gate lengths varied from 200 to 700 nm and the finger width from 50 to 150 µm. Fig. 2 shows a schematic cross

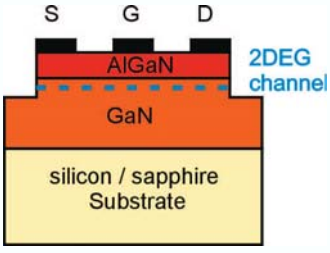

Fig. 2
Schematic cross section of an AlGaN/GaN HEMT

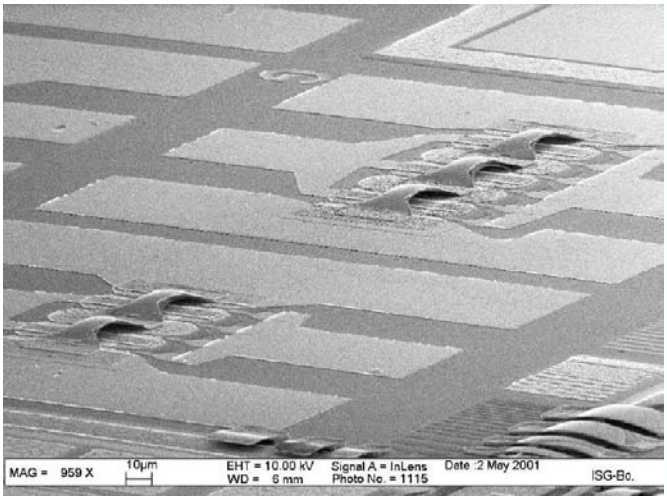

Fig. 3
SEM photograph of AlGaN/GaN/sapphire multi-finger HEMTs with 4 and 6 gates, LG = 450 nm, w = 50 µm.

section of the transistors. In the case of 4- and 6-finger devices an air-bridge is used to connect the source contacts (Fig. 3). These devices are planned for power applications.

RESULTS

The output characteristics of HEMTs with 200 nm gate length are depicted in Fig. 4. Self-heating effects reduce the drain current and the transconductance at high drain voltages. The HEMTs on silicon substrates show a much weaker current decrease than a sapphire based devices. This is due to the higher

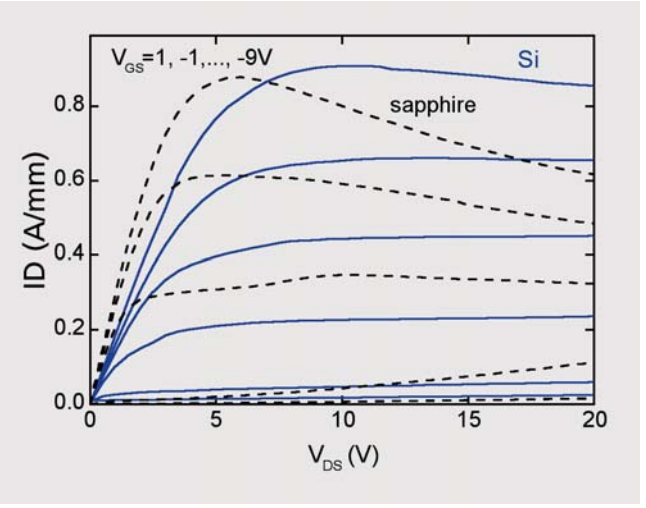

Fig. 4
Comparison of HEMTs on sapphire and Si substrate (L_G = 200 nm), showing the influence of the substrate on the current decrease by self-heating

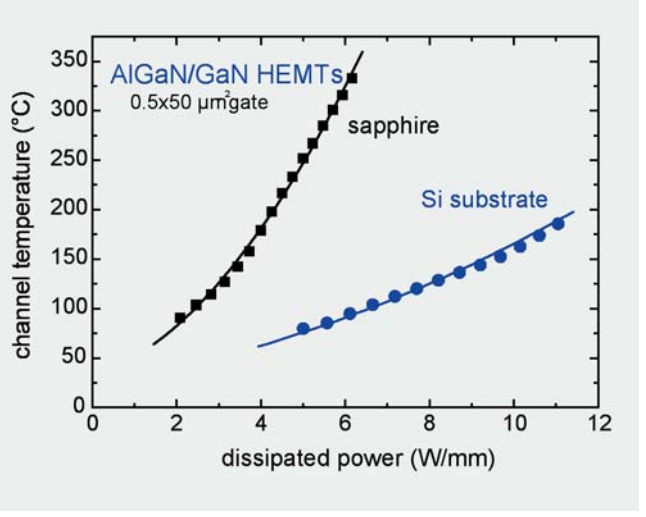

Fig. 5
Channel temperature as function of dissipated dc power

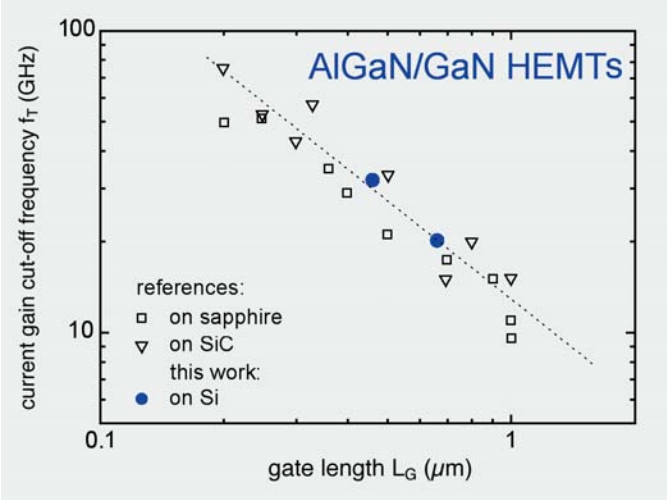

Fig. 6
Cutoff frequency of AlGaN/GaN HEMTs for different gate lengths

thermal conductivity of silicon (1.5 W/cm K), if compared to sapphire (0.35 W/cm K). The temperature dependence of the source resistance is used to determine the channel temperature of the HEMTs as function of the dissipated dc power [2]. The results demonstrate the superiority of the silicon substrate (Fig. 5). More gate fingers or a wider gate increase the self-heating effects for both substrates. This must be considered when the layout is scaled up for high power transistors. The silicon based AlGaN/GaN HEMTs with 500 nm gate length show a cutoff frequency (f_T) of 32 GHz and a maximum frequency of oscillation (f_{MAX}) of 27 GHz. These values are the highest reported so far for AlGaN/GaN/Si HEMTs [3]. The f_{MAX} to f_T ratio is only 0.85 compared to a ratio of 2 for devices with the same geometry and similar layer structure grown on sapphire. This indicates the influence of the parasitic conduction through the Si substrate under small signal conditions. Thus, the use of Si substrates with a higher resistivity will further improve the RF performance of AlGaN/GaN/Si HEMTs. Fig. 6 shows the cutoff frequencies for different substrate materials. The presented silicon based HEMTs are fully comparable to devices fabricated on sapphire or SiC substrates. This strongly suggests the future use of silicon substrates for the fabrication of AlGaN/GaN HEMTs for power applications, leading to significant cost advantages.

REFERENCES

[1] "AlGaN/GaN HEMTs on (111) Silicon Substrates",
P. Javorka, A. Alam, M. Wolter, A. Fox, M. Marso, M. Heuken, H. Lüth, and P. Kordoš,
IEEE Electron Dev. Lett. 23 (2002) 4.

[2] "Determination of Channel Temperature in AlGaN/GaN HEMTs Grown on Sapphire and Silicon Substrates using DC Characterization Method"
J. Kuzmík, P. Javorka, A. Alam, M. Marso, M. Heuken, and P. Kordoš,
IEEE Trans. Electron Dev. 49 (2002) 1496.

[3] "AlGaN/GaN HEMTs on Silicon Substrates with f_T of 32/20 GHz and f_{max} of 27/22 GHz for 0.5/0.7 µm Gate Length"
P. Javorka, A. Alam, A. Fox, M. Marso, M. Heuken, and P. Kordoš,
Electron. Lett. 38 (2002) 288.

AUTHORS

Michel Marso, Peter Javorka, Peter Kordoš